Monthly Notices of the ROYAL ASTRONOMICAL SOCIETY

MNRAS **508,** 79–99 (2021) https://doi.org/10.1093/mnras/stab2273
Advance Access publication 2021 August 6

Linear spectropolarimetric analysis of fairall 9 with VLT/FORS2

Bo-Wei Jiang [1,2★] Paola Marziani [3] Đorđe Savić [4,5] Elena Shablovinskaya [6] Luka Č. Popović [5,7] Victor L. Afanasiev [6] Bożena Czerny [8] Jian-Min Wang [1,2,9] Ascensión del Olmo [10] Mauro D'Onofrio [11] Marzena Śniegowska [8,12] Paola Mazzei [3] and Swayamtrupta Panda [8,12]

[1] *Key Laboratory for Particle Astrophysics, Institute of High Energy Physics, Chinese Academy of Sciences, 19B Yuquan Road, Beijing 100049, China*
[2] *School of Astronomy and Space Science, University of Chinese Academy of Sciences, 19A Yuquan Road, Beijing 100049, China*
[3] *INAF, Osservatorio Astronomico di Padova, Vicolo dell'Osservatorio 5, I-35122 Padova, Italy*
[4] *Institut d'Astrophysique et de Géophysique, Université de Liège, Allée du 6 Août 19c, B-4000 Liège, Belgium*
[5] *Astronomical Observatory, Volgina 7, 11060 Belgrade, Serbia*
[6] *Special Astrophysical Observatory, Russian Academy of Sciences, Nizhnij Arkhyz 369167, Russia*
[7] *Department of Astronomy, Faculty of Mathematics, University of Belgrade, Studentski trg 16, 11000 Belgrade, Serbia*
[8] *Center for Theoretical Physics, Polish Academy of Sciences, Al. Lotników 32/46, PL-02-668 Warsaw, Poland*
[9] *National Astronomical Observatories of China, Chinese Academy of Sciences, 20A Datun Road, Beijing 100020, China*
[10] *Glorieta de la Astronomia s/n, Instituto de Astrofisíca de Andalucía, IAA-CSIC, E-18008 Granada, Spain*
[11] *Dipartimento di Fisica & Astronomia 'Galileo Galilei', Università di Padova, I-35122 Padova, Italy*
[12] *Polish Academy of Sciences, Nicolaus Copernicus Astronomical Center (PAN), ul. Bartycka 18, 00-716 Warsaw, Poland*

Accepted 2021 July 30. Received 2021 July 9; in original form 2021 May 5

ABSTRACT

The quasar main sequence appears to be an incredibly powerful tool to organize the diversity in large samples of type-1 quasars but the most important physical parameters governing it are still unclear. Here, we investigate the origin of the broadening and of a defining feature of Population B sources: a strong redward asymmetry of the Balmer emission lines. We focus on a prototypical source, Fairall 9. Spectropolarimetric data of the Fairall 9 broad H β and H α profiles allowed for a view of the geometric and dynamical complexity of the line emitting regions. Measurements (1) provided evidence of rotational motion; (2) were helpful to test the presence of polar and equatorial scatterers, and their association with non-virial motions. However, we suggest that the polarization properties appear to be more consistent with a warped disc geometry induced by Lense–Thirring precession.

Key words: line: profiles – techniques: polarimetric – quasars: emission lines – quasars: individual: Fairall 9 – quasars: supermassive black holes.

1 INTRODUCTION

The quasar main sequence (MS) is a concept that arose from the principal component analysis on 87 quasars introduced by Boroson & Green (1992). The usefulness of the MS is rooted in the ability to contextualize every quasar as part of a sequence (Sulentic, Marziani & Dultzin-Hacyan 2000a; Shen & Ho 2014). Most notable correlations involve the width and shape of the Balmer line profiles, the strength of optical Fe II emission and the amplitude of the systematic blueshifts of high-ionization lines with respect to the quasars rest frame (see e.g. Fraix-Burnet et al. 2017, for a summary). Eventually, the Eigenvector 1 (E1)-related correlations allowed for the identification of two main quasar populations along the MS: Population A (Pop. A) with full width at half-maximum (FWHM; H β) ≤ 4000 km s^{-1} and Population B (Pop. B) with FWHM (H β) $>$ 4000 km s^{-1} (Sulentic et al. 2000a).

The physical parameters governing the MS are still being investigated, although some basic inferences have been made. The main parameters that describe quasars as accreting black holes are the black hole mass ($M_{\rm BH}$, ranging from 10^6M$_\odot$ to $10^{9.5}$M$_\odot$; Kormendy & Richstone 1995), the accretion luminosity, Eddington ratio ($L_{\rm Bol}/L_{\rm Edd}$, Boroson & Green 1992; Sulentic et al. 2000b; Marziani et al. 2001, 2003b), and the black hole spin (e.g. Wang et al. 2014). The $M_{\rm BH}$ can be estimated by assuming that the gas motions are predominantly Keplerian around the black hole, and by applying the virial theorem for a system whose mass is entirely concentrated in the center of gravity. Reverberation mapping provides a measurement of the radial distance $r_{\rm BLR}$ of the line emitting gas from the central black hole (Peterson 1993, 2004). The so-called 'virial mass' have been computed for large samples of quasars employing several different emission lines, various measures of line width, and exploiting correlation between the emitting region radius and luminosity (see Marziani & Sulentic 2012; Shen 2013; Popović 2020, for reviews). An independent method relies on the scaling law between $M_{\rm BH}$ and the stellar velocity dispersion of the galaxy bulge ($\sigma_\star$; Kormendy & Ho 2013). Recently, spectropolarimetric observations of the Hydrogen Balmer lines have allowed to measure the intrinsic line FWHM due to a Keplerian velocity field and to compute the black hole mass independently from orientation (Afanasiev & Popović 2015; Afanasiev, Popović & Shapovalova 2019, and references therein). All methods to compute black hole mass in active galactic nucleus

★ E-mail: jiangbw@ihep.ac.cn

(AGN) are subject to caveats and suffer considerable uncertainties (e.g. Dalla Bontà et al. 2020, and references therein). None the less, the $L_{\rm Bol}/L_{\rm Edd}$, which is proportional to the luminosity-to-black hole mass ratio ($L/M_{\rm BH}$), has been revealed to be a fundamental driver of the E1 MS, closely related to several observational parameters (Marziani et al. 2001, 2003b; Kuraszkiewicz et al. 2004; Shen & Ho 2014; Panda et al. 2018; Panda, Marziani & Czerny 2019). With decreasing Eddington ratio, source properties change from the ones of Pop. A to the ones of Pop. B, which tend to show broader Balmer emission lines, weaker $R_{\rm FeII}$,[1] and more asymmetric Balmer line profiles (Sulentic et al. 2000b; Marziani et al. 2003b; Shen & Ho 2014).

Apart from the Eddington ratio, several studies found that the orientation effects can influence the FWHM of Balmer lines in type-1 quasars as well (e.g. Wills & Browne 1986; Rokaki et al. 2003; Sulentic et al. 2003; Jarvis & McLure 2006; Decarli, Dotti & Treves 2011; Panda et al. 2019). In this sense, Pop. B sources might be seen at a larger viewing angle (defined as the angle between the line of sight and the accretion disc axis; Marziani et al. 2001; Shen & Ho 2014). Other factors influence the line widths in addition to orientation, most notably $M_{\rm BH}$, and $L_{\rm Bol}/L_{\rm Edd}$. From the position of a source in the optical plane of the MS, FWHM (H β) versus $R_{\rm Fe\,II}$, it is not possible to retrieve unambiguous evidence on the viewing angle. This is an unfortunate occurrence, as there is observational and theoretical support for a highly flattened low-ionization emitting region (e.g. Mejía-Restrepo et al. 2018, and references therein).

In addition to broader line profiles, Pop. B sources tend to have red-ward asymmetries in Balmer emission lines (see e.g. Boroson & Green 1992; Marziani et al. 1996; Sulentic et al. 2002; Punsly 2010; Wolf et al. 2020). Several studies have found out that the H β emission line profiles can be empirically modeled by a very-broad component (VBC) with a typical width ($\gtrsim$ 10 000 km s^{-1}), twice as broad as the classical broad component (BC; Sulentic et al. 2000a). The VBC shift is yielding the observed asymmetry (Marziani et al. 2003a). The physical explanation of the unshifted BC involves a virialized, optically thick gaseous region (Snedden & Gaskell 2007; Czerny & Hryniewicz 2011; Wang et al. 2017; Marziani et al. 2018). The VBC can be explained as due to a high ionization, at least in part virialized region closer to the central black hole [called the very broad line region (BLR; Peterson & Ferland 1986; Brotherton et al. 1994; Popović et al. 1995; Sulentic et al. 2000a; Popović et al. 2004; Snedden & Gaskell 2007; Wang & Li 2011; Marziani et al. 2019)].

The projection effect due to different viewing angles of BLR and the physical origin of the red-ward asymmetry are still enigmatic at the time of writing. Spectropolarimetric studies provide a powerful tool for probing the geometry of the BLR (Smith et al. 2005; Afanasiev et al. 2014, 2019; Baldi et al. 2016). The polarized light, scattered from an equatorial dusty torus, contains structural and kinematic information for both the BLR and the scattering region (Smith et al. 2005). The measurement of the Stokes parameters, the polarization degree (P per cent), the polarized flux ($P \times F$), and the polarization position angle (PA) can in principle be used for estimating the mass of the central SMBHs in a way that is independent of the viewing angle (Afanasiev & Popović 2015; Savić et al. 2018, 2020; Songsheng & Wang 2018; Afanasiev et al. 2019), as a potential tracer of super-massive binary black holes as well as of non-virial motion (Savić, Marin & Popović 2019).

Fairall 9 (≡ ESO 113–45; Fairall 1977) is a Seyfert 1 galaxy at a comoving radial distance of ≈195.3 Mpc, with a luminous nucleus ($M_V = -22.6$; Véron-Cetty & Véron 2010). Optical spectroscopy in the H β spectral range indicates that Fairall 9 is a prototypical Pop. B quasar, with FWHM of the virialized H β BC at 4550 km s^{-1} and $R_{\rm FeII} \lesssim 0.5$ (Marziani et al. 2010). Moreover, it has a moderate redward asymmetry that can be modeled with a VBC shifted to the red in Ly α, C IV, Mg II, and H β emission lines (Marziani et al. 2010).

In this paper, we present analysis of the new spectropolarimetric observations of Fairall 9 AGN with the aim to investigate the innermost part and to ascertain the origin of the broadening and of the redward asymmetry of the H α profile observed in this object. More details on the source are reported in Section 2. We then present the analysis of spectropolarimetric data obtained using the Very Large Telescope (VLT; Section 3). Main results from parameters measured on the polarization spectrum are described in Section 4. Results point to a more complex scenario than a single-disc Keplerian motion and an equatorial scattering. They are discussed and interpreted with the help of ray-tracing programs in Section 5. Throughout the paper, we adopt a ΛCDM cosmological model with $H_0 = 70$ km s^{-1} Mpc^{-1}, $\Omega_{\rm M} = 0.3$, and $\Omega_\Lambda = 0.7$.

2 FAIRALL 9: A PROTOTYPICAL POPULATION B SOURCE

Since the time of its identification, Fairall 9 has been considered a favored target because of its brightness in the infrared (IR), optical, UV, and X-ray domains. At first, it was so because Fairall 9 was believed to be an 'extreme' Seyfert 1 where extreme meant that it was bordering the luminosity range of quasars. The host galaxy is well-resolved, classified as S0 by the APM Bright Galaxy Catalogue (Loveday 1996), more likely SB0a on a visual inspection of the ACS image shown by Bentz et al. (2009), with a faint companion (LEDA 5109) located at 30 arcsec SSW from Fairall 9. The angular separation corresponds to ∼30 kpc of projected linear distance. Fairall 9 is definitely radio quiet, as it was not detected by the Sydney University Molonglo Sky Survey (Mauch et al. 2003) with a detection limit of 6 mJy, implying a ratio radio-to-optical specific flux $\lesssim 1.5$.

Reverberation mapping campaigns in the optical (Santos-Lleó et al. 1997) and in the UV (Vestergaard & Peterson 2006) have provided measurements of the BLR radius $r_{\rm BLR}$ from both low- and high-ionization lines. Previous estimates of black hole mass based on the reverberation-mapping method converge to values $(1.5-2.5) \times 10^8 {\rm M}_\odot$ (Peterson et al. 2004; Bentz & Katz 2015), depending on the adopted virial factor. A conventional estimate of the bolometric luminosity for Fairall 9 is $\log L_{\rm Bol} \approx 45.3$ erg s^{-1}, and the Eddington ratio $\log (L_{\rm Bol}/L_{\rm Edd}) \approx -2.0$ (Marziani et al. 2010), close to the low end in the distribution of Pop. B sources (Marziani et al. 2003b). Revised estimates of these parameters are provided in Section 5.5.

Line shifts with respect to rest frame are of special importance to this investigation. The rest frame we assumed is based on the measured redshift of Fairall 9, $z = 0.046\,09 \pm 0.000\,02$ (heliocentric redshift is $z_\odot \approx 0.046\,05$) measured on a 1993 ESO spectrum published in Marziani et al. (2003a), from the narrow component (NC) of H β and from [O III]λλ4959,5007).[2]

The MS empirical parameters reveal that the spectral type of Fairall 9 is B1, one of the most populated along the MS of quasars (Sulentic

[1]Defined as the ratio of the intensity of Fe IIλ4570 blend to the intensity of H β BC.

[2]The 10 km s^{-1} heliocentric correction is not relevant considering the scale of the polarization spectrum is ≈ 4 Å/pix ≈ 180 km s^{-1}.

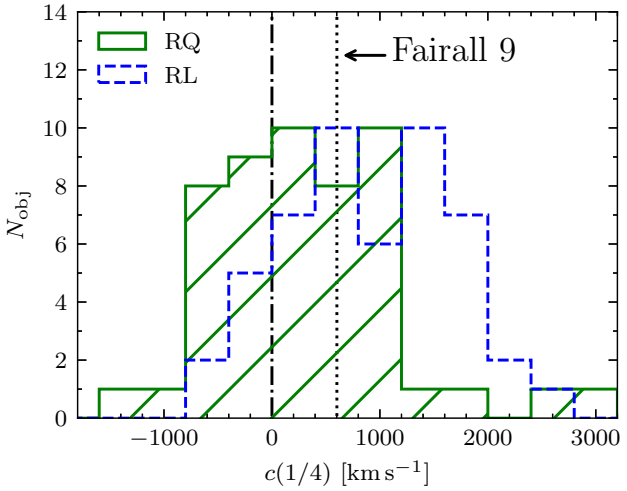

Figure 1. The measured H β centroid at 1/4 of the maximum, based on the sample of Marziani et al. (2003a) of 101 Pop.B objects. The green histogram refers to the distribution of 51 radio-quiet (RQ) objects, while the blue histogram represents the 50 radio-loud (RL) sources. The $c(1/4)$ of Fairall 9 is ≈600 km s^{-1} marked as dotted line in the plot. The 0-velocity shift is marked as dotted-dash line. The bin size is 400 km s^{-1} for both RQ and RL sources, and was set on the basis of the typical uncertainty in the $c(1/4)$ estimates.

et al. 2000b; Marziani et al. 2003b; Shen & Ho 2014), consistently associated with low L_{Bol}/L_{Edd}. Following Zamfir et al. (2010), we define the centroid shift with respect to the rest frame at 1/4 maximum $c(1/4) = (v_B(1/4) + v_R(1/4))/2$, where $v_B(1/4)$ and $v_R(1/4)$ refer to the velocity shift on the blue and red wing at 1/4 of the peak intensity, respectively. The $c(1/4)$ is a measurement of the line profile displacement with respect to the rest frame and its value measured on the H β profile of Fairall 9 is ≈ 600 km s^{-1} close to the average and median values for the Pop. B RQ sample of Marziani et al. (2003a, shown in Fig. 1).[3] The spectral energy distribution (SED) is also consistent with objects of Pop. B with no strong big-blue bump. In the X-ray domain, Fairall 9 has a flat spectrum ($\Gamma = 2.0$), with photon index from the 0.5 to 40 keV $\Gamma = 1.8$–2.0 (Lohfink et al. 2016). The X-ray spectrum has been interpreted as due to a power law, continuum components (including a modest soft X-ray excess) associated with cold and ionized blurred reflection (Emmanoulopoulos et al. 2011; Walton et al. 2013).

3 OBSERVATIONS, DATA REDUCTION, AND POLARIZATION ANALYSIS

3.1 Observations

The FOcal Reducer and low dispersion Spectrograph 2 (FORS2) is installed at the Cassegrain focus of ESO's VLT. The spectrograph has been designed for multiple purposes in visible and near-UV bands, including a polarimetric mode. The polarimetric mode allows the measurement of linear polarization. A Wollaston prism is introduced as beam splitter in the optical path, and a super-achromatic half-wave retarder plate connected to a grism with slitlets and a filter make it possible to carry out spectropolarimetry (ESO 2019).

[3]http://vizier.u-strasbg.fr/viz-bin/VizieR?-source = J/ApJS/145/199

For our observations, we used the GRIS_300V grism and the order separation filter GG435 to fully cover the H β and H α profile, and approaching a spectral resolution ∼800 in the wavelength range of H α, with a step of ≈ 4 Å/pix. The observation of Fairall 9 was carried out during the night of 2018 November 7, with seeing condition $\lesssim 1$ arcsec. The half-wave retarder plate was rotated at angles of $0°, 22.5°, 45°$, and $67.5°$. At every individual PA, a set of six observations was taken, each with an exposure of 240 s. The centroid of the target was placed in one of the Multi-Object Spectroscopy movable slitlets, with the height set to 11.4 arcsec. The produced spectra were split into ordinary (o) and extraordinary (e) beams by the Wollaston prism, and recorded on the CCD with a separation of about 22 arcsec (the pixel scale in the spatial direction is $D_s = 0.126$ arcsec / pixel (ESO 2019).

3.2 Data reduction

We performed the standard procedure of the spectropolarimetric data reduction described in details in Afanasiev & Amirkhanyan (2012) and adopted to the VLT/FORS2 data. The reduction process includes the following steps: bias subtraction and extraction of the frames from the original fits-files, construction of the 2D model of the geometrical distortions for ordinary and extra-ordinary ray spectra, spectra linearization using He-Hg-Cd-Ar arc lamp spectrum and flat-field correction and night sky lines subtraction. The effective spectral range is 4400–7500 Å.

The o- and e-beam spectra were extracted using a fix aperture size of around 40 pixels. The size of the aperture was chosen so that the nucleus flux was totally integrated within the seeing on each exposure.

3.3 Polarization analysis

The formulæ to calculate the normalized Stokes parameters in the general form can be found in Patat & Romaniello (2006). Here, we will use the relations adopted for the case of the measuring of the polarization with the Wollaston prism and rotating λ/2 plate given in Afanasiev & Amirkhanyan (2012):

$$\begin{aligned} Q(\lambda) &= \frac{1}{2}\left(F(\lambda)_{\theta=0°} - F(\lambda)_{\theta=45°}\right), \\ U(\lambda) &= \frac{1}{2}\left(F(\lambda)_{\theta=22.5°} - F(\lambda)_{\theta=67.5°}\right), \end{aligned} \tag{1}$$

where θ is the PA of the retarder plate and $F(\lambda)$ is the normalized flux difference between the ordinary ($f_o(\lambda)$) and extraordinary ($f_e(\lambda)$) beams:

$$F(\lambda) = \frac{f_o(\lambda) - f_e(\lambda)}{f_o(\lambda) + f_e(\lambda)}. \tag{2}$$

Linear polarization degree P and polarization PA are related to the Stokes parameters as:

$$\begin{aligned} P(\lambda) &= \sqrt{Q(\lambda)^2 + U(\lambda)^2}, \\ \mathrm{PA}(\lambda) &= \frac{1}{2}\arctan\frac{U(\lambda)}{Q(\lambda)}. \end{aligned} \tag{3}$$

The $\pi/2$ ambiguity of the polarization angle is corrected according to the formulae given in Bagnulo et al. (2009).

3.3.1 Atmospheric depolarization

The atmospheric depolarization, caused by non-selective aerosol light scattering, has a serious effect on the results of the

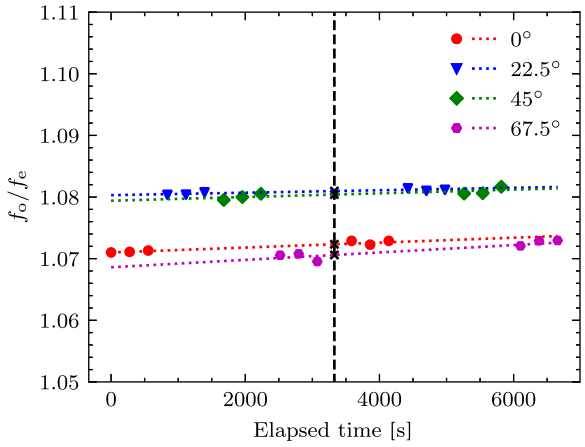

Figure 2. The change of depolarization coefficients in polarizing channels during observations for different retarder angles. The scatters are the average ratio in each frame. The dotted lines show the tendency of the ratio. Black dashed line is at the middle of observation with cross mark showing the speculative depolarization coefficients.

spectropolarimetric analysis. From the data we collected, the effect could reach up to 1 per cent (shown in Fig. 2). To eliminate such effect, we followed procedures discussed in Afanasiev & Amirkhanyan (2012). We assumed the depolarization effect is wavelength independent, and we considered the depolarization during the exposure as a variation of the spectrograph transmission for the ordinary and extraordinary rays. In this case, we used

$$F(\lambda) = \frac{D(\theta_i) f_o(\lambda) - f_e(\lambda)}{D(\theta_i) f_o(\lambda) + f_e(\lambda)} \quad (4)$$

instead of the expression in equation (2), where $D(\theta_i)$ are the coefficients of the polarization transmission channels which also include the variations of the atmospheric depolarization. As it can be found in Afanasiev & Amirkhanyan (2012), these coefficients are usually obtained for each retarder PA and for each exposure. Due to the non-optimal observational technique, we had to use the time-averaged coefficients which are calculated as:

$$D(\theta_i) = \langle f_o(\lambda)/f_e(\lambda) \rangle \quad (5)$$

where the angle brackets correspond to the averaging over the time. Correction because of atmospheric (de)polarization should be applied every time the ratio between the ordinary and extraordinary beam intensity is shown to depend on time. Even a change of ≈1 per cent can yield to a large difference in the polarization angle.

3.3.2 *Interstellar polarization*

The interstellar matter (ISM), including molecular gas and dust, can have a considerable effect on the linear polarization because of scattering (Whittet et al. 2001). The observed polarization is a vectorial composition of the polarization of the target and ISM, and the corresponding Stokes parameters U and Q have the relation as:

$$(Q, U)_{\rm obs} = (Q, U)_{\rm AGN} + (Q, U)_{\rm ISM} \quad (6)$$

To determine and eliminate the ISM polarization, we used three low-polarized stars (Heiles 2000) close to Fairall 9. Their polarization data are in Table 1. We assume that all three stars are non-polarized, and that their observed polarization is entirely caused by ISM scattering. Even assuming this one can clearly see that the polarization of the nearby stars is equal to zero within the very low errors. So, we will consider further that the interstellar polarization is negligible in the direction of Fairall 9.

3.3.3 *Instrumental polarization*

To correct the bias of the mean level of the Stokes parameters calculating from the given spectropolarimetric data, we need to correct the data for the instrumental polarization. Because no standard star of zero polarization was obtained at the night of Fairall 9 observations, the zero level of the instrumental polarization was defined from the spectra of the host-galaxy of the object. For this, we integrated the frames of the spectra in the range out of the object aperture. Assuming the instrumental polarization independent from the wavelength, we obtained: $Q_{\rm ins} = 0.8, U_{\rm ins} = -0.1$. The instrumental values were subtracted from the Stokes parameters of the object.

4 RESULTS

4.1 Natural light decomposition

We first decomposed the Hα and Hβ emission line profile in natural light (shown in Fig. 3). A minimum-χ^2 analysis using the IRAF task `specfit` (Kriss 1994) was carried out to include all the relevant components in the Hα spectral region from 6200 to 7000 Å with a power-law AGN continuum, host galaxy continuum, Hα emission components, narrow forbidden lines of [O I]λ6300, [O I]λ6363, [N II]λλ6548, 6584, and [S II]λλ6717,6730. As for Hβ, the fitting was carried out in the spectral range from 4430 to 5550 Å, including a power-law AGN continuum, host galaxy continuum, Hβ emission components, the Fe II emission blends, the narrow forbidden lines [O III]λλ4959, 5007, He IIλ4686 emission, and Gaussians accounting for the blended emission of several high-ionization iron forbidden lines peaking at λ ≈ 5200 Å ([Fe VI]λ5146, [Fe VII]λ5159, [Fe VI]λ5176, [Fe IV]λ5236, [Fe VII]λ5276, and [Fe XIV]λ5302). Since the host contamination of Fairall 9 is relatively weak with

Table 1. Low-polarized star properties.

RA (h:m:s) (1)	DEC (d:m:s) (2)	P (per cent) (3)	PA (°) (4)	Q (per cent) (5)	U (per cent) (6)
$01^h06^m54^s.46$	$-59°58'01''.2$	0.016 ± 0.023	110.0 ± 35.7	−0.012 ± 0.022	−0.010 ± 0.021
$01^h31^m32^s.58$	$-59°35'34''.4$	0.012 ± 0.014	83.9 ± 30.3	−0.012 ± 0.014	0.003 ± 0.013
$01^h35^m14^s.71$	$-58°08'21''.5$	0.015 ± 0.012	97.1 ± 21.8	−0.015 ± 0.012	−0.004 ± 0.011

The three low-polarized stars from Heiles (2000). Column 1: right ascension. Column 2: declination. Columns 3 and 4: polarization degree(P) and polarization PA reported in the literature. Column 5 and 6: the decomposed Stokes parameters Q and U computed from Column 3 and 4 based on equation (3). All the uncertainties reported here are at 1σ confidence level.

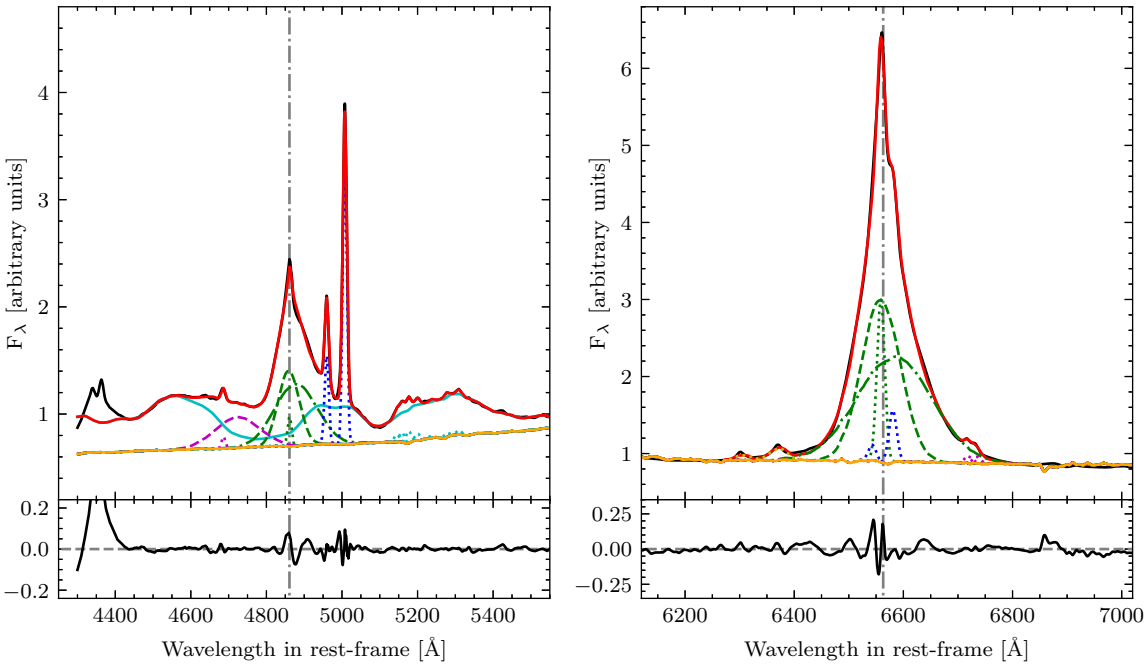

Figure 3. Decomposition of the Hβ (left-hand panels) and Hα (right-hand panels) natural light profiles with multiple components. The grey dot–dashed line marked the rest frame for Hβ and Hα, respectively. Top-left panel: the fitting range for Hβ, 4430–5550 Å. The observed total flux is in solid black line while the best-fitting result is shown in red. The sum of the power-law continuum and the host galaxy component is shown as an orange line. The Fe II blends modeled with the template are plotted in solid cyan line. Green dashed, dot–dashed and dotted lines represent the decomposed BC, VBC, and NC for Hβ, respectively. Blue dotted lines are [O III]$\lambda\lambda$4959, 5007. He IIλ4686 emission are modeled with a VBC (magenta dashed line) and a NC (magenta dotted line). Dotted cyan lines stand for the high-ionization iron forbidden lines in the range 5100–5300 Å. Top-right panel: the fitting range for Hα, 6200–7000 Å. The black, red, and orange solid lines have identical meaning as in left-hand panel. Green dashed, dot–dashed and dotted lines represent the decomposed BC, VBC, and NC for Hα, respectively. Blue dotted lines are [N II]$\lambda\lambda$6548, 6584. Yellow dotted lines are [O I]λ6300 and [O I]λ6363. Magenta dotted lines represent [S II]$\lambda\lambda$6717,6730. Bottom panels are the residual for the fitting with grey dashed lines marking the zero levels.

respect to the active nucleus continuum, the host galaxy component in natural light has been modeled using the spectrum of the elliptical galaxy NGC 3379 (Kennicutt 1992). The Fe II emission templates are based on I Zw 1 from Boroson & Green (1992). The decomposition of the Hα profile proper involved three Gaussians (Fig. 3): (1) the narrow component (NC), (2) the BC, (3) the VBC which has a substantial peak shift to the red by $\sim$ 1000 km s^{-1}, and accounts for the redward asymmetry of the Hα full broad profile (i.e. BC + VBC). The decomposition of Hβ also involved three Gaussians (see also Fig. 3): (1) one NC, (2) one BC, (3) one VBC that is shifted to the red by $\sim$2000 km s^{-1}, leading to a more expanded red wing in the total Hβ profile.

In radio-quiet (RQ) Pop. B sources, C IVλ1549 shows a systematically stronger blue side with respect to the Balmer line profiles. The excess is small and much lower than in several cases of extreme Pop. A sources that have blueshifted emission dominating the C IVλ1549 profile (e.g. Leighly & Moore 2004; Marinello et al. 2020, for examples). The origin of the blue excess in natural light is often considered to be due to outflowing gas, possibly in the form of a wind, dense clumps, or dense clumps embedded in a wind (see e.g. Kollatschny 2003; Proga 2003).

A *HST*/FOS spectrum was extracted from the MAST archive and reduced by Sulentic et al. (2007) who provide measurements of the C IV line intensity and profile parameters. The C IV λ1549 profile of Fairall 9 has been reanalysed in this work, with special attention to the line wings. We carried out the decomposition of the C IV λ1549 based on *HST*/FOS UV spectra following the approach developed in Marziani et al. (2010). We consistently used the same components

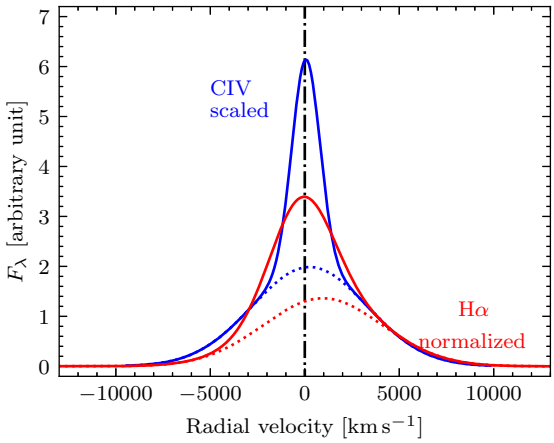

Figure 4. Hα (red) and C IVλ1549 (blue) profiles overlaid after rescaling of C IVλ1549 to the same intensity of the Hα red wing. Hα and C IVλ1549 VBC are shown by dotted red and blue lines, respectively.

in the fitting procedure, i.e. one NC, one BC, and one VBC. The result is shown in Fig. 4. Compared to Hα, C IV seems to be more symmetric, with a redshifted VBC at only a few hundred km s^{-1}. This is mainly caused by two unresolved Gaussian components shifted to blue and red, respectively (Marziani et al. 2010). Since the redshifted component is slightly more prominent, we can see a modest redward asymmetry in total flux. Now to help the interpretation of the Hα

profile, we superimpose and rescale the red-wing of C IV and Hα at the same intensity (Fig. 4). Both Hα and C IV have outstanding redward asymmetries. The red side of C IV is consistent with the one of Hα, but with a revealing difference: the centroid at 1/4 peak intensity $c(1/4)$ is 194 ± 199 km s^{-1} for C IV and 442 ± 136 km s^{-1} for Hα, where the uncertainties are at a 2σ confidence level. If the red wings are matched, the blue side of C IV is somewhat more extended, making the C IV profile more symmetric especially close to the line base: the shift to the red of the $c(1/4)$ is only marginally significant. This implies that the C IV is affected by a small blueshifted excess, most likely associated with outflowing gas.

4.2 Polarization of the BLR

After the correction for the atmospheric depolarization, ISM, and instrumental polarization, we derived the polarization parameters using the method described in 3.3. The results are presented in Fig. 5.

The total intensity profiles of Hβ and Hα lines are shown in panel 1 of Fig. 5. As the contribution of the narrow lines ([O III] and [N II]) will depolarize the broad lines slightly but their wrong estimation will cause much larger inaccuracies, the NCs were not subtracted from the spectra. Note here that the atmospheric absorption B-band affects the profile of Hα line between 6860 and 6917 Å.

The second and third panels in Fig. 5 show the Stokes parameters Q and U binned over the 15 Å window. For each spectral bin, we estimated the robust average of the measured values over the spectral range and all taken exposures. The errors given on the plots are equal to the 1σ level, where σ is the robust standard deviation.[4]

The polarization degree P is plotted at the fourth panel in Fig. 5. The Hα and Hβ lines show values of the polarization percentage P per cent ≈ 0.05 per cent (Hβ) – 0.12 per cent (Hα) lower than the one of the average adjacent continuum polarization ($\approx$1.07 per cent).

The profiles of the polarization PA are shown on panel 5 of Fig. 5. In both the Hβ and Hα lines, one can detect a double 'swing': the profiles change within around $\pm 10^\circ$ relatively to the mean level that the continuum polarization shows, with minimum PA around -7000 km s^{-1}. These features point out the presence of the equatorial scattering in the nucleus region, according to Smith et al. (2005), and the detection of such profiles in both lines is a strong evidence in favour of this model. This inference is consistent with the Pop. B nature of Fairall 9 i.e. with Fairall 9 belonging to the 'disc dominated' type-1 AGN (Richards et al. 2002). Following the paper by Afanasiev & Popović (2015), we examine below these profiles in details to estimate the viewing angle and the black hole mass, and to finally resolve the velocity field of the gas emitting the reflected radiation.

5 DISCUSSION

Appendix B provides STOKES and SKIRT models for several geometric and kinematic configurations. The sketch of Fig. B1 shows a Keplerian disc, a polar outflow region, a spherical BLR, and a double disc surrounded by the equatorial scatterer – a dusty torus. In the first part of the discussion, we will describe the comparison between these and other competing models and the data, beginning with the possibility of polar scattering, while in the second part we will focus on the analysis of the models that are suggested by the data. For the quantitative χ^2 comparison, we consider only Hβ up to $+5000$ km s^{-1} (beyond this radial velocity, the [O III] doublet destroys the polarization profile of broad Hβ). The Hα profile is more heavily affected by the Hα NC, by [N II] emission, and by the B band within $|\delta v_r| \lesssim 2000$ km s^{-1}, right where S/N is higher. The Hα polarization profiles gave always worse χ^2_ν than Hβ, but the main features of Hα profile are qualitatively consistent with the main features of Hβ. Hα is therefore used for confirmatory purposes. The most robust, salient feature that we need to explain is the almost constant polarization degree across the Hβ and Hα profile, which in turns lead to a single-peaked polarized flux profile. The second main feature is the PA profile, whose 0 point is apparently displaced from rest frame. In this respect, Fig. 6 shows average and weighted average of the Hβ and Hα PA data. A significant change in PA is not occurring at $v_r \approx 0$ km s^{-1}, but at $v_r \approx -2750$ km s^{-1}: a Welch t-test yields a significance $\sim(1 - 3 \times 10^{-4})$ for the change in PA between the radial velocity averages over the range -6000 to -3000 km s^{-1} and -3000 to $+2500$ km s^{-1} (blue and black lines in Fig. 6). The absence of a 'swing' centered at $v_r \approx 0$ km s^{-1} is also visible in Figs 5 and A2 for both Hβ and Hα, and their average is reinforcing the result at a statistical level.

5.1 Polar scattering

In the previous discussion, we have assumed that the scattering region is equatorial, with relatively small inclination with respect to the symmetry plane offered by the accretion disc. However, this assumption may not be fully adequate. For Pop. B sources like Fairall 9, the inclination is relatively large. It is reasonable to consider the effect of polar scattering as done by Smith et al. (2004). In the interpretation of Smith et al. (2004) of sources showing evidence of both polar and equatorial scattering, the polar scattering region is subdivided into (1) a scattering cone aligned with the emission disc axis, but with a very large opening angle as shown in fig. 10 of Smith et al. (2004); (2) a spherical wedge at large inclination (but still low enough for the line of sight not to intercept the torus). If the main component of the polar scatterer is distributed in this configuration, we can expect that the width of the polarized flux feature and of the swing PA pattern will be narrowed, polarization degree lowered, and that PA might be different in the continuum and in the line.

A combination of polar and equatorial scattering appears, in principle a possibility. This would not have been a first occurrence by far. A combination of polar and equatorial scattering is expected as a general feature of type-1, where the polar scattering electrons are provided by gas in correspondence of the narrow-line region (Smith et al. 2004). This could make it possible to form a central peak in the polarization profile. The inclination estimates imply that the line of sight may pass close to the edge of the torus. However, Fairall 9 is a very low polarization object, with no sign of significant reddening and highly polarized continuum, suggesting that it should be seen well above the torus (and with the line of sight not passing through the wedge). The source is different from Fairall 51, the prototypical 'Seyfert on the edge.' In addition, if a polar scatterer is assumed as in region (1) of Smith et al. (2004), we should see evidence of narrowing in the polarized flux feature and in the swing PA pattern, which we don't: the swing PA pattern is wide.

5.2 Model inter-comparison

Fig. 7 shows the data superimposed to the best fits from the models discussed below. The minimum normalized χ^2_ν values obtained from

[4]Note here that we are applying the basic robust estimation using 2σ rejection threshold to avoid the influence of the outlier points in the observational data set. The algorithm implementation could be found in more details in Press et al. (2007), and references therein.

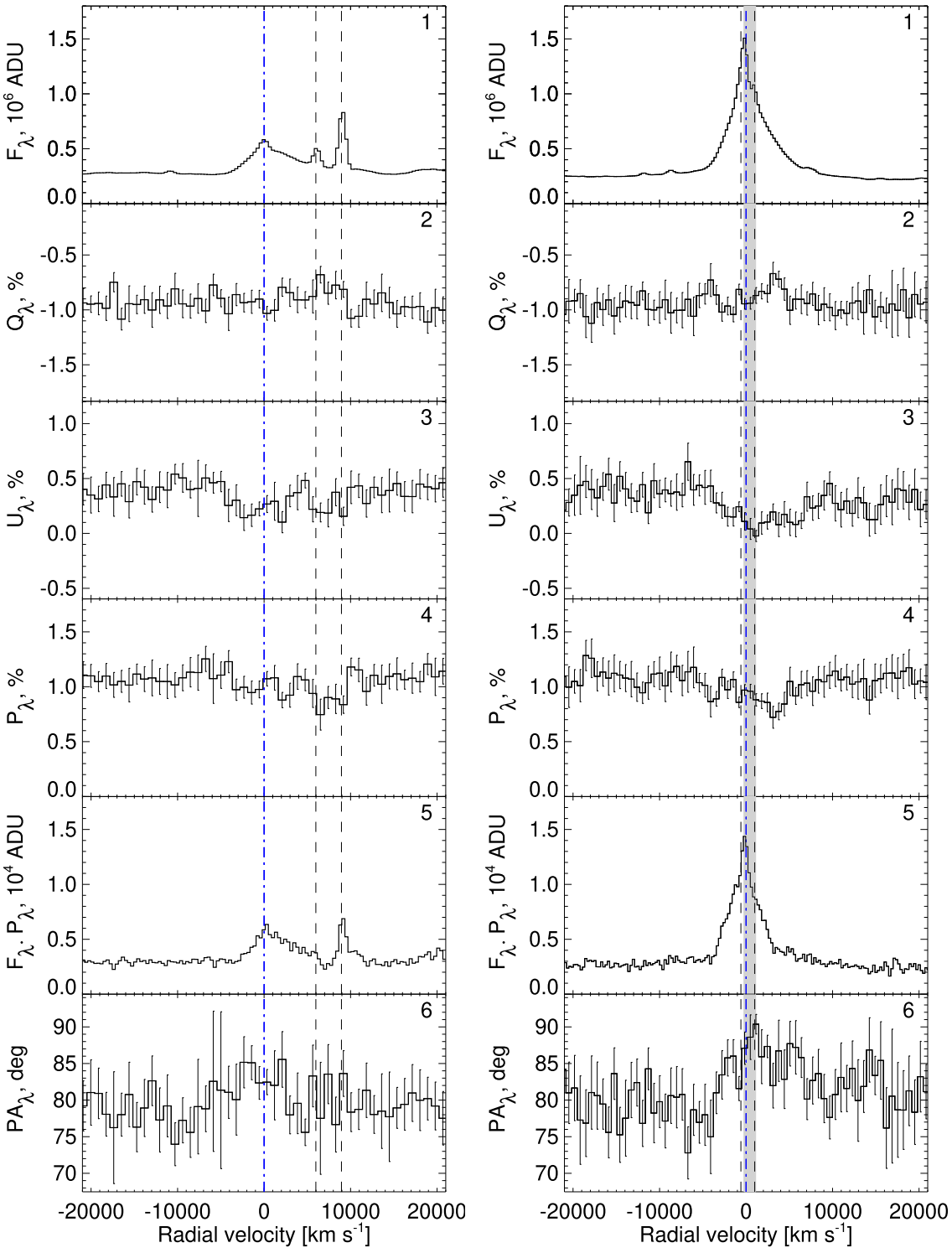

Figure 5. The profiles of H β (left) and H α (right) lines. From top to bottom: the intensity in the natural light, the Q and U Stokes parameters, the polarization degree, the polarized flux, and the polarization angle. The values on panels 1 and 5 are binned in 6 Å window and the values on panels 2–4 and 6 – in 15 Å window. The black vertical dashed lines mark the narrow lines coming from the NLR – [O III] lines at H β profile and [N II] lines at H α profile. The blue vertical dashed line marks the position of zero velocity. For H α, the atmospheric absorption band is noted with a light grey stripe. Error bars are at 1σ confidence level.

the model best fits to the data are reported in each panel. The continuum polarization has been added and the polarization per cent predicted by the model has been scaled by a free factor to obtain a minimum χ^2. They are computed in the range $-10\,000 \leq v_r \leq 6000$ km s^{-1}. Beyond 6000 km s^{-1}, there is evidence of depolarization associated with the narrow [O III] emission. Considering that the number of degrees of freedom is 16, for most models, an F-test based on the normalized χ^2_ν ratios for the different models would require

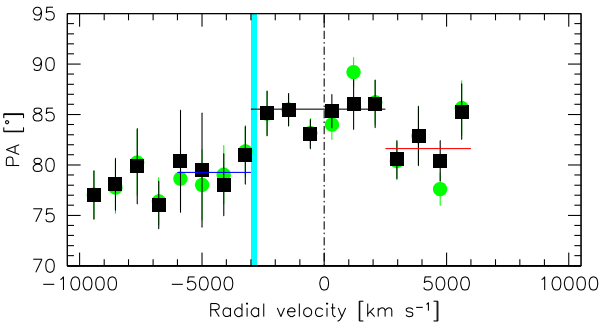

Figure 6. The PA as a function of radial velocity, for the average (black squares) and weighted average (green squares) of the Hβ and Hα PAs. Horizontal lines trace the average values of the PA over three ranges in radial velocity. The cyan stripe identifies the range over which a significant change in PA occurs, around -2750 km s^{-1}.

a minimum $F(1,2) = \chi^2_{\nu,1}/\chi^2_{\nu,2} \approx 1.268$ for detecting a difference that is significant at a 1σ confidence level. The minimum χ^2_ν is often consistent with a flat or almost flat behaviour, which might imply a very low polarization degree associated with a low optical depth of the scatterer. To show the behaviour expected for each model, the grey histogram line in Fig. 7 traces the model predictions in an arbitrary scale.

5.2.1 *Single disc model + equatorial scatterer*

Having excluded polar scattering, we turn to the Keplerian disc and equatorial scatterer model that we implicitly applied for the $M_{\rm BH}$ estimate. This is the model that has been successfully applied to several tens of type-1 AGN (Afanasiev et al. 2019). It shows a typical double-swing feature of PA with the $\rm PA_{max}$ amplitude decreasing as the viewing inclination increases. The polarized line is broader than the line in natural light and the degree of polarization shows double-peaked profiles with maxima in the wings and minimum in the core (Fig. B2). However, the polarized flux profile of Fairall 9 is single peaked for both Hβ and Hα. The polarization percentage across the profiles changes little, and may indicate a different situation from the simple case of the rotational motion in a flat disc and equatorial scatter. Fig. 7 shows that the agreement between data and model is fair. The χ^2 is not very high for both the polarization per cent and the polarization PA. The single disc profile seen at an inclination of $\approx$30 degrees is consistent with the data for both the P per cent and the PA, supporting the presence of rotational motions.

No improvement is obtained if a blueshift of about $\approx$2500 km s^{-1} is imposed to the disc model. This ad hoc modification is suggested by the PA profile that is not symmetric around 0, as already shown in Fig. A2. A shift would significantly lower the Hα PA χ^2. However, for Hα, the improvement in the polarization angle is not accompanied by a corresponding agreement in the polarization per cent profile, and for Hβ there is no significant improvement.

5.2.2 *Spherical BLR*

The spherical BLR model involves an isotropic velocity dispersion along with the spherical geometry. The typical double-swing feature of PA is visible also in this case, and the models of the single Keplerian disc and the spherical BLR give similar results. The agreement is again fair. A shift to the blue by ≈ -2000 km s^{-1} improves the polarization per cent profile, at the expense of a worsening of the PA χ^2_ν.

5.2.3 *Outflows*

We considered a model for which the BLR geometry follows a bi-conic outflow with constant velocity (Fig. B1, top second panel, Zheng, Binette & Sulentic 1990; Marziani et al. 1996; Corbett et al. 2000). Such model produces a clear double-peaked unpolarized lines, while the polarized line is highly asymmetric with blue part being dominant towards intermediate viewing angles, while the red part is dominant towards pole-on view. The Stokes parameter U is antisymmetric with respect to the line center, while Q is asymmetric, which results in asymmetric double-swing PA profiles. The bi-conic model provides the minimum χ^2_ν among all models, but the fit of the PA profile is poor, and disfavoured at a 1σ confidence level. Bi-conical outflows require high Eddington ratio and may therefore be specific of sources accreting at higher rate than Fairall 9.

Pop. B sources also show evidence of outflows as discussed in Section 4, even if less powerful than in Pop. A. We consider two alternatives. The first outflow in the scattering medium located at the inner edge of the torus (in the previous models the scatterer was assumed stationary) yields a poor χ^2. As in the case of the single disc, the model predicts two peaks in the per cent of polarization that are not observed. The model with an outflowing scatterer overlying the disc emission could be interpreted as a disc wind, perhaps driven by magneto-hydrodynamical forces (Emmering, Blandford & Shlosman 1992). Unlike the cases studied by Lira et al. (2020), the agreement with our data is not good: the χ^2_ν of the P per cent profile is consistent with unity (even if the minimum χ^2_ν obtained for a flat profile), but the PA profile is not favoured.

5.2.4 *Double Keplerian disc*

We simplified the warped disc with a combination of two disc-like BLRs at two inclinations (the two-disc model): the inner disc corresponding to region (2) is rotated by an angle of 30° around the x-axis with inner and outer radius of 1000–2000 $r_{\rm g}$. The outer disc (region 1) is situated in the asymptotic plane that contains the equatorial plane of the torus (Fig. 8) and extends from 2000 to 10 000 $r_{\rm g}$. Region 3 is represented as the point-like source of the continuum. The models of Fig. 3 provide qualitative confirmation of the feature seen in the Fairall 9 spectrum. Fig. 7 shows the polarization parameters predicted for two inclined disc configuration (third row from top). It is interesting to note that the inclination of the inner disc of the model (45°) is consistent with the angle estimated by Lohfink et al. (2012) using X-ray spectra ($\sim$48°). The warp geometry might imply that the innermost disc emitting the X-continuum and the inner disc in the model may be facing each other (Fig. 8).

The main features observed in the polarization profile of Fairall 9 are recognizable in the models.

(i) The polarized flux in Fig. 5 shows a centrally peaked structure. The two-disc models shown in the Figs B2 and B3 of Appendix B show the sum of two concentric 'rings' and clearly represent an oversimplification with respect to the reality of a warped disc. A real warped disc can be assimilated to a sequence of narrow rings with inclination progressively closer to the one of the Kerr black hole equatorial plane, easily producing a single peaked polarization profile. The point here is that a flat polarization percentage profile within $\pm$5000 km s^{-1} yields a polarized flux profile that is centrally

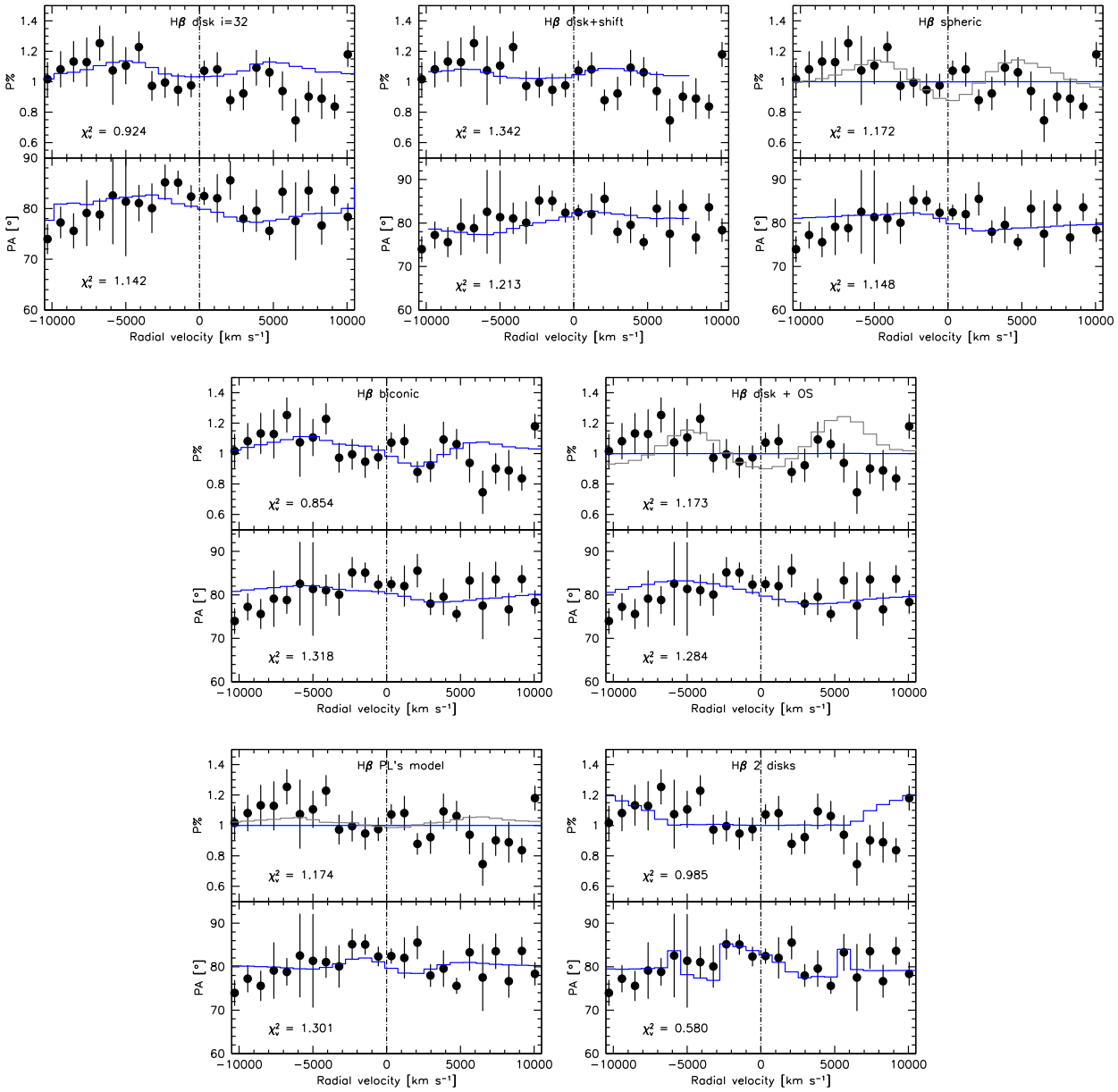

Figure 7. Comparison between several ray-tracing models and the observational data for H β. Each panel is split in half; the top one shows the polarization percentage and the bottom one the polarization PA. Top row, from left to right: results for a single disc geometry and equatorial scattering, for a single disc geometry to which an arbitrary shift has been added, and for a spherical geometry. Second row from top: biconical outflow model, disc with outflow motion of the scatterer by 500 km s^{-1}, and a disc + 4000 km s^{-1} scatterer outflow, with the scatterer overlying the emission disc as developed by Lira et al. (2020). The third row are the results for a two-disc model with the two discs inclined by 30° with respect to each other, with the outer disc observed at 15°.

peaked as the profile in natural light (panel 5 of Fig. 5). This behaviour is qualitatively consistent with the polarized flux profile expected for a warped disc, and is not consistent with the one expected from a single rotating disc and an equatorial stationary scatterer.

(ii) Negative ΔPA in the radial velocity range from $-10\,000$ to -3000 km s^{-1} are predicted by models and are qualitatively consistent with the change observed in the data (bottom panel of Fig. 5).

(iii) The shape of the PA around 0 km s^{-1} is predicted by the model if the disc at $\phi \approx 0°$–$45°$, Fig. 7 can also explain the observed PA shape that suggests a change in the sign in the polarization angle at non-zero radial velocities.

Fig. 7 shows the model overlaid to the data point. The χ^2_ν is the lowest among the different model, and best agreement is obtained for the azimuthal angle $\phi = 15°$ case. A $\chi^2_\nu \approx 0.99$ is obtained for the P per cent of the two disc model. It is just a factor 1.15 larger than the χ^2_ν obtained for the biconic model and, according to the *F*-test criterion, not significantly different. The PA profile of the two-disc model has a significantly lower χ^2_ν with respect to all other cases, at least by a factor $\gtrsim 2$, implying that the difference is significant at a confidence level of more than 1σ, and close to 90 per cent.

The innermost part of the BLR is expected to be seen at inclination $\gtrsim 30°$ (and significantly different from the 10–15° inferred for the outer disc), because of the relatively modest ΔPA in the swing that

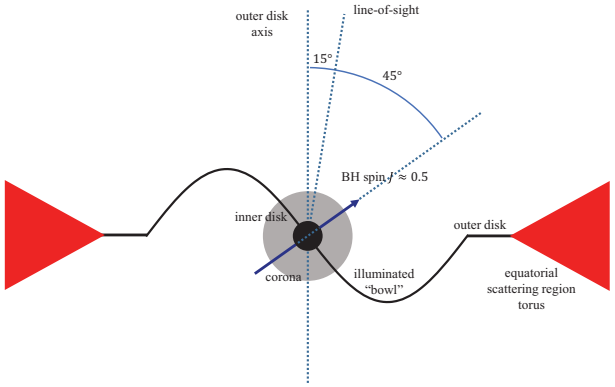

Figure 8. Sketch (not drawn to scale; the curvature of 'bowl' is greatly exaggerated, and there should be no discontinuity between the outer and inner disc, see Fig. 9) illustrating the warped disc geometry suggested in this paper.

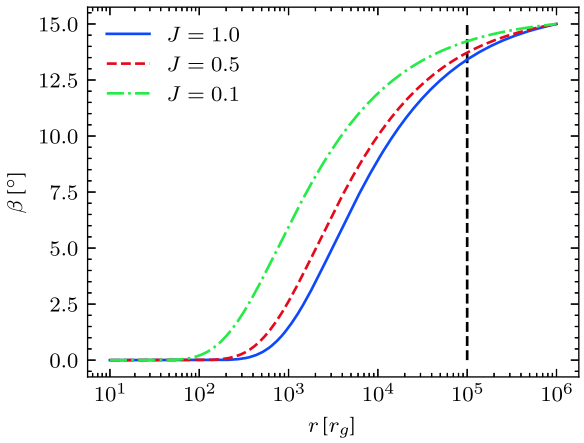

Figure 9. The solution of equation (9) in Bardeen & Petterson (1975) with different angular momentum J in units of $M_{\rm BH}{}^2$. The tilt angle β is normalized to 15° at $10^6\,r_{\rm g}$. Other parameters in the equation are set to unity.

implies relatively high values of the viewing angle. A warp can indeed change the viewing angle of the line emitting region in the innermost part of the BLR, lowering the swing amplitude. Fig. B2 shows that the amplitude of the swing is decreasing with viewing angle (Smith et al. 2005). If these effects are taken into account, the $M_{\rm BH}$ derived from spectropolarimetry might be underestimated.

However, the polarized flux predictions consistent with a warped disc and the agreement with the two-disc model PA profile suggest that a two-disc system or a warped disc might be the most appropriate models.

5.3 A transient second disc

The model that produces best agreement with the data involves two discs at different inclinations with respect to the line of sight. A tidal disruption event (TDE) could have given rise to a second accretion disc. Fairall 9 has been described as a changing look AGN in recent papers. It has passed from a very low state in the early 1980s (Kollatschny & Fricke 1985); however, in the low state the broad lines almost never disappeared. Although TDEs are relatively short lived, and destined to fade in the course of a few years, there are claims of longer events (Lin et al. 2017). In the case of Fairall 9, the V observations of the ASAS-SN (Shappee et al. 2014) indicate remarkable photometric stability over the period May 2014–September 2018, with an average $V \approx 13.77$ mag and a dispersion of just ≈0.07 mag. We suggest that the strong change occurred in the 1980s might be a 'long-term event of sustained accretion' (Trakhtenbrot et al. 2019). These events might be typical of AGN, and especially among Pop. B sources accreting at relatively low rates.

5.4 A warped disc

Apart from a second disc due to a TDE, the only mechanism known to us that may yield a change in disc orientation on the spatial scale of the inner BLR is Lense–Thirring precession, produced by the misalignment between the spin of the black hole and the angular momentum vector of the accreting gas (Bardeen & Petterson 1975).

The expectations for a warped structure involve three main regions: (1) an outer, asymptotic disc with a well-defined tilt angle of the plane of the disc relative to the equatorial plane of the black hole β_0; (2) an intermediate region where inclination β can be much larger than β_0; (3) a region within $\lesssim 100$ gravitational radii where the disc is in the equatorial plane of the rotating black hole. The third region is probably too hot to account for the observed emission line spectrum. It is more likely to host the X-ray corona (Begelman, McKee & Shields 1983; Haardt & Maraschi 1993; Różańska & Czerny 2000), and be the source of most UV and X continuum. See Fig. 8 for a schematic representation of a warped structure tentatively adjusted to the observational constraints on Fairall 9.

Modeling the exact geometry of a warped disc is difficult since three Euler angles are needed to define the orientation of a warped structure in space. In the warped disc scenario, the inflection on the natural line profile of Hα roughly separates two regions: the outer one (region 1), Keplerian, still in the plane of the accreting gas, and an innermost one more inclined, exposed to the full strength of the AGN continuum, and producing the high-ionization VBC (region 2; the illuminated 'bowl' of Fig. 8; see Bachev (1999) for a computation of the detailed illumination and self-shadowing patterns in a warped disc geometry). Assuming $M_{\rm BH} \approx 2 \times 10^8$ M$_\odot$, the radial BLR distance measured from reverberation mapping corresponds to $\approx 1700\,r_{\rm g}$. A change of inclination can be induced, on a spatial scale of $\sim 10^3\,r_{\rm g}$ by Lense–Thirring precession (Bardeen & Petterson 1975).

The trends of Fig. 9 represent the behaviour of the inclination angle of the warped disc β as a function of the radial distance in units of gravitational radii for $J = 0.1$, 0.5, 1, and are expected for Lense–Thirring precession as computed by Bardeen & Petterson (1975). The Lense–Thirring scale is consistent with the linear scale derived from $r_{\rm BLR}$. It is also interesting to see that we expect a strong increase in the inclination of the disc at a few hundred gravitational radii from the black hole, and that inclination of the disc start deviating from the one of the equatorial plane of the black hole at smaller distances for lower J. This is in turn expected to increase the direct illumination of the disc by the central UV/X continuum source, known to be very low in the case of a geometrically thin disc (see e.g. section 5.10 of Frank, King & Raine 2002).

The gravitational + transverse redshift in the VBC goes as $\delta z \approx \frac{3}{2} r_{\rm g}/r$ (Bon et al. 2015). Therefore, the VBC emission could be strongly affected by gravitational redshift: the rotational velocity scales with $r^{-\frac{1}{2}}$, implying that $r \approx (c/v)^2 r_{\rm g}$. For a rotational velocity $v \sim 15\,000$ km s^{-1}, $r \approx 450\,r_{\rm g}$, and we obtain a gravitational + transverse redshift ∼1000 km s^{-1}. Fig. 9 shows that the β value remains close to 0 up 400 $r_{\rm g}$ for the case of a maximally rotating black hole ($J \approx 0.994$, Thorne 1974). If $J < 1$, as mentioned, the maximum

radius at which the disc plane lies in the equatorial plane of the black hole should be lower. Therefore, gas at very small radii could be more efficiently illuminated, and the emitted radiation should be even more strongly affected by gravitational redshift with $J < 1$ than with $J \approx 1$. A Suzaku measurement of the Fairall 9 spin yields $J \approx 0.60 \pm 0.07$ (Schmoll et al. 2009).

A Kerr black hole is in principle capable of producing a rotation of the polarization plane via the 'gravitational Faraday effect' (Ishihara, Takahashi & Tomimatsu 1988). The effect is achromatic, but strongly dependent on the distance from the central black hole: the rotation $\delta\mathrm{PA} \approx \frac{5}{4}\pi m J \cos\theta_0 / r_{\mathrm{min}}^3$, where m is the mass of the black hole in the natural units, r_{min} is a photon impact parameter, and θ_0 is the angle between the spin of the black hole and the line of sight. Assuming $r \sim 100\,m$, $J \sim 1$, $\cos\theta_0 \sim 1$, the δPA $\ll 1^\circ$. Even if recent numerical simulations suggest a larger effect (Chen et al. 2015), a significant δPA ($\sim 10^\circ$) is possible only at $r \lesssim 10 r_{\mathrm{g}}$, i.e. for photons in the X-ray domain.

Invoking a warped disc presents several drawbacks. Warps are expected to be rare, as they require special conditions: rejuvenation of a black hole from gas whose angular momentum is not aligned with black hole spin. Large systematic redshifts and blueshifts should be equally possible (Wang & Li 2012), as the illuminated bowl of a warped disc would lose axial symmetries (Bachev 1999). The large shifts and irregular profiles predicted by kinematical models are relatively rare (but large blueshifts are found; see several examples in Zamfir et al. (2010), while the Balmer line profiles of Fairall 9 are fairly typical for a Pop. B object). However, the redward asymmetry might be *always* associated with gravitational redshift (see in this respect Popović et al. 1995; Corbin 1995), and a warped geometry may contribute to make it more evident, as the bowl shape should make it possible to efficiently expose the line emitting gas at a few hundreds gravitational radii.

5.4.1 Fairall 9: analogies and differences with E 1821 + 643 and Mark 668

The broad emission Balmer lines of E 1821 + 643 show an unusual shape with a highly red asymmetric profile and a large broad line peak redshifted ($\sim$1000 km s^{-1}) relative to the narrow lines (see Shapovalova et al. 2016). However, E 1821 + 643 is a striking example of profile reversal in polarized light, where to a prominent redward asymmetry corresponds a prominent blueshifted excess in polarized light (Smith et al. 2002) explained by the emission of one active component of a binary super-massive BH or a recoiling black hole after collision (Robinson et al. 2010). As done by Robinson et al. (2010), we identify two components in the BLR, one with 0 or a smaller redshift, and one broader with a larger redshift ($\sim$2000 km s^{-1}). However, considering that the features can be identified in most Pop. B sources (about 50 per cent of quasars), it seems unlikely that they could be due to a bulk motion of the BLR with respect to the host galaxy. Since the broader feature is ascribed to the inner most part of the emitting regions, profile reversal in natural light (i.e. the redward asymmetry turning into a blue one or profile turning from asymmetric to symmetric or vice versa) should be expected on time-scales of a few years. The first published spectrum of sufficient quality was obtained in 1977 (Hawley & Phillips 1978); the Hβ profile is remarkably similar to the one of the observations in 2019. Over a 42 yr time lapse the total displacement is significantly larger than the BLR distance from the central continuum source: $\approx 2.65 \times 10^{17}$ cm, assuming a constant velocity of 2000 km s^{-1}. If the original BLR radius was $\approx 1.44 \times 10^{17}$ cm, the recoiling displacement added to the original radius implies that the ionization parameter of the gas 'left behind' in the BLR should be lower by a factor 0.1, and that there should have been a decrease in the Hα and Hβ BC intensity with respect to the VBC by a factor $\approx$0.38, assuming the same, typical conditions for the BLR. There is no positive evidence of this decrease [for an account of the variability pattern, see Lub & de Ruiter (1992)]. Kollatschny & Fricke (1985) reported the almost disappearance of the broad Hβ emission between 1981 and 1983, but afterwards the AGN bounced back to its pre-1981 spectrum. Further monitoring on a time-scale of a decade should provide a stringent test on the recoiling black hole hypothesis.

Mrk 668 (OQ 208) is known since long because of a redshifted peak by $\sim$2600 km s^{-1} in the natural light profile of Hβ (Gezari, Halpern & Eracleous 2007, and references therein). The peak radial velocity has remained approximately constant since the first report on the shifted feature, over 40 yr ago (Osterbrock & Cohen 1979). In this case, the presence of a black hole binary is not supported by the data (Doan et al. 2020). The spectropolarimetric data are consistent with $b = -0.5$ suggesting a predominance of Keplerian motion. The ΔPA changes sign at $\delta v_{\mathrm{r}} \sim 0$, as in the case of Fairall 9 (Afanasiev et al. 2019).

A warped disc geometry is affected by self shadowing, as the disc illumination is strongly dependent on the azimuthal angle ϕ. Single peaks highly displaced to both the red and blue are predicted for the Balmer line profiles in natural light (Bachev 1999; Wu, Wang & Dong 2008). In the case of Mrk 668, optical Fe II emission shows a consistent shift with the Balmer lines (Bon et al. 2018), providing additional evidence supporting that we are seeing low-ionization emission lines from a virialized, Keplerian system, with the Fe II emission occurring predominately at the outer edge of the disc, as expected (Panda et al. 2020, and references therein). On the ground of the stability of the profile over a time-scale longer than the dynamical time-scale of the BLR, and of its spectropolarimetric properties, we suggest that OQ 208 could be considered as a warped disc candidate.

5.5 M_{BH} and $L_{\mathrm{Bol}}/L_{\mathrm{Edd}}$ estimate for Fairall 9

5.5.1 M_{BH}

The details of the M_{BH} computations following the spectropolarimetric and other methods are reported in Appendix A. The various estimates reported in Table A2 disagree by a factor almost 3, within the range $M_{\mathrm{BH}} \approx (1.2 - 3.3) \times 10^8$ M$_\odot$. Each method has some strong point but also some difficulties. The spectropolarimetric mass estimate depends on the distance of the scatterer, which in turns depends on scaling laws connecting it to luminosity (Table A2). The weighted average of the M_{BH} values reported in Table A2 from spectropolarimetry is $M_{\mathrm{BH}} \approx (1.49 \pm 0.48) \times 10^8$ M$_\odot$. It is doubtful whether the Afanasiev et al. (2019) method can be applied in warped disc geometry. Indeed, the uncertainty in the a parameter rather large, $\delta a \approx 0.13$ and $\approx$0.15 for Hβ and Hα, respectively, if compared to the typical uncertainties reported by Afanasiev et al. (2019), always $\lesssim 0.12$. However, the spectropolarimetric estimate compares well with the average from the application of the virial relation using r_{BLR} from reverberation mapping,[5] as reported in Table A2, even if it is significantly lower than the estimate obtained from two scaling laws based on the Hα FWHM, and especially from the width of the Si absorption line at 1.59 μm, which indicate

[5]The RM estimates rely on the virial factor, which is not well constrained in the case of Fairall 9.

$M_{\rm BH} \gtrsim 2 \times 10^8$ M$_\odot$. We computed a median and weighted average black hole mass considering all methods (even if they are not fully independent). The median $M_{\rm BH} \approx (1.68 \pm 0.48) \times 10^8$ M$_\odot$ (with the semi-interquartile range as uncertainty) and the weighted average $M_{\rm BH} \approx (1.71 \pm 0.63) \times 10^8$ M$_\odot$ are both consistent with the $M_{\rm BH}$ derived from spectropolarimetry, and also with the previous determination of Recondo-Gonzalez et al. (1997).

The Pop. B $M_{\rm BH}$ distribution at low-z covers the black hole mass range $8 \lesssim \log M_{\rm BH} \lesssim 10$ [M$_\odot$], in flux-limited samples built on long-slit or fiber optical spectroscopic observations (Shen et al. 2011; Marziani et al. 2003b). This result would place Fairall 9 towards the low end of the $M_{\rm BH}$ distribution for Pop. B. However, these samples are subject to a strong selection bias, as sources with a relatively small black hole mass ($M_{\rm BH} \sim 10^6$ M$_\odot$) radiating at low Eddington ratio are increasingly lost even at modest redshift. Very recently, the MANGA survey (Yan et al. 2016) has made it possible to detect low-luminosity, type-1 AGN associated with black hole mass even in the intermediate $M_{\rm BH}$ domain (Mezcua & Domínguez Sánchez 2020; Hernandez-Toledo et al., in preparation). The loss of Pop. B sources is also relevant at high redshift, as the flux limit of large surveys introduces an Eddington ratio-dependent cut off at any given $M_{\rm BH}$ (Sulentic et al. 2014).

5.5.2 L_{Bol}/L_{Edd}

The bolometric luminosity of Fairall 9 has been estimated as $L_{\rm Bol} \sim 4.75 \times 10^{45}$ erg s^{-1} by integrating the observed SED. The SED for Fairall 9 is provided by Brown et al. (2019), which includes photometric and spectroscopic observations of the AGN ranging from 2.5×10^{-5} to $9.6 \cdot 10^2$ μm. The Eddington luminosity can be written as $L_{\rm Edd} = 1.5 \times 10^{38} (M_{\rm BH}/M_\odot)$ erg s^{-1}. For $M_{\rm BH} \approx 2 \times 10^8$ M$_\odot$, the Eddington ratio is $L_{\rm Bol}/L_{\rm Edd} \sim 0.16$, consistent with Pop. B but close to the limit. The observations of Brown et al. (2019) refer to a period when the source was in a high state; assuming the flux of Bentz et al. (2009; also consistent with the average of the Santos-Lleó et al. 1997 monitoring campaign) corrected for the host galaxy contribution would imply a bolometric luminosity $L_{\rm Bol} \sim 1.65 \times 10^{45}$ erg s^{-1}, and an Eddington ratio $\approx$0.06. The variability notwithstanding, Fairall 9 has remained within the limit of Eddington ratio associated with Pop. B ($\approx$0.2).

6 CONCLUSION

Using VLT/FORS2 we obtained spectropolarimetric observations of the RQ Pop.B source Fairall 9. The measured polarization properties have been used for inferring constraints on the kinematics and geometry of the BLR as well as on the scattering region. Our results on the spectropolarimetric properties of Fairall 9 can be summarized as follows.

(i) Fairall 9 shows low degree of polarization in correspondence of the Balmer H β and H α emission lines. The polarized flux profiles of both lines are centrally peaked.

(ii) The polarization angle in the center of H β and H α is atypical, in the sense that the 'swing' shape is not as regular as the one seen in most cases by Afanasiev et al. (2019), and the dynamical center may be shifted with respect to rest frame.

(iii) We consider several scenarios from the Monte Carlo, ray-tracing code STOKES and SKIRT: disc-like BLR, bipolar outflowing BLR, spherical BLR, and two-disc BLR. The minimum χ^2 in ΔPA is obtained for the two-disc case.

(iv) The agreement with the two-disc hypothesis indicates that the inner disc may be tilted with respect to the outer disc, and that emission from the VBC may be associated with the inner disc.

(v) The possibility of a second disc originating from a tidal-disruption event is not favoured on the ground of the photometric behaviour of Fairall 9 right in the 4 yr preceding the spectropolarimetric observations.

(vi) Excluding the possibility of a TDE-produced disc, the most likely hypothesis appears to be a warped structure driven by Lense–Thirring precession. Models support the possibility that a double disc structure may be at the origin of the PA, polarized flux, and polarization percentage behaviour.

(vii) Using the width of the polarized broad H β and H α profile, we estimated the inclination and the central black hole mass. The inclination effect plays a significant role in the emission line broadening especially in Pop. B sources. For Fairall 9, the inclination angle cannot be determined as easily as for other sources, but is constrained around 50°. The corresponding virial factor is $\approx$2. The derived values are consistent with the expected role of the viewing angle along the FWHM axis in the optical plane of the E1 MS (Marziani et al. 2001; Panda et al. 2019). However, if a warped structure is present, then to consider a single value of the viewing angle could be misleading.

(viii) The central black hole mass obtained by using the spectropolarimetric method of Afanasiev et al. (2014) is somewhat lower with respect to the mass estimates from most other methods, which give an average $M_{\rm BH} \sim 2 \times 10^8M_\odot$. However, The slope b is consistent with the value expected for predominance of a Keplerian velocity field.

If our inferences are correct, the case of Fairall 9 confirms the dominance of Keplerian motions in the BLR of Pop. B sources. The issue of orientation is complicated by the warped structure revealed in this source. The results on Fairall 9 further strengthen the hypothesis that gravitational redshift might be the governing factor of the VBC redshift, due to the easy illumination of the disc gas in a warped geometry (in this respect, Punsly et al. (2020) suggest that at very low $L_{\rm Bol}/L_{\rm Edd}$, the effect of gravitational redshift is strong because only the innermost part of the disc is illuminated by the AGN continuum). Deep, high-resolution observations of other Pop. B sources are however needed to test whether the spectropolarimetric results obtained for Fairall 9 may be common and general.

ACKNOWLEDGEMENTS

The authors thank the reviewer whose suggestions and comments helped improve the paper. BWJ would like to express sincere gratitude to the Astrophysical Observatory of Asiago, Italy, where most of the preliminary work in this paper was efficiently carried out, thanks to the pleasant and quiet working place and accommodation they generously provided. BWJ and JMW acknowledge financial support from the National Natural Science Foundation of China (11833008 and 11991054), from the National Key Research and Development Program of China (2016YFA0400701), from the Key Research Program of Frontier Sciences, Chinese Academy of Sciences (CAS; QYZDJ-SSW-SLH007), and from the CAS Key Research Program (KJZD-EW-M06). VLA and ES thank the grant of Russian Science Foundation project number 20-12-00030 'Investigation of geometry and kinematics of ionized gas in active galactic nuclei by polarimetry methods', which supported the spectropolarimetric data analysis. ĐS and LČP acknowledge funding provided by the Astronomical Observatory Belgrade (the contract 451-03-68/2020-14/200002) through

the grants by the Ministry of Education, Science, and Technological Development of the Republic of Serbia. This work was supported by the F.R.S.–FNRS under grant PDR T.0116.21. AdO acknowledges financial support from the Spanish grants MCI PID2019-106027GB-C41 and the State Agency for Research of the Spanish MCIU through the 'Center of Excellence Severo Ochoa' award for the IAA (SEV-2017-0709). Under the same award, PM acknowledges the Hypatia of Alexandria visiting grant. This research has made use of the NASA/IPAC Extragalactic Database (NED) which is operated by the Jet Propulsion Laboratory, California Institute of Technology, under contract with the National Aeronautics and Space Administration. This work is based on data collected at Paranal Observatory under programme 0102.B-0743(A).

DATA AVAILABILITY

The data underlying this article will be shared on reasonable request to the corresponding author.

REFERENCES

Afanasiev V. L., Amirkhanyan V. R., 2012, Astrophys. Bull., 67, 438
Afanasiev V. L., Popović L. Č., 2015, ApJ, 800, L35
Afanasiev V. L., Popović L. Č., Shapovalova A. I., Borisov N. V., Ilić D., 2014, MNRAS, 440, 519
Afanasiev V. L., Popović L. Č., Shapovalova A. I., 2019, MNRAS, 482, 4985
Assef R. J. et al., 2011, ApJ, 742, 93
Bachev R., 1999, A&A, 348, 71
Baes M., Peest C., Camps P., Siebenmorgen R., 2019, A&A, 630, A61
Bagnulo S., Landolfi M., Landstreet J. D., Land i Degl'Innocenti E., Fossati L., Sterzik M., 2009, PASP, 121, 993
Baldi R. D., Capetti A., Robinson A., Laor A., Behar E., 2016, MNRAS, 458, L69
Bardeen J. M., Petterson J. A., 1975, ApJ, 195, L65
Begelman M. C., McKee C. F., Shields G. A., 1983, ApJ, 271, 70
Bentz M. C., Katz S., 2015, PASP, 127, 67
Bentz M. C., Peterson B. M., Netzer H., Pogge R. W., Vestergaard M., 2009, ApJ, 697, 160
Bon N., Bon E., Marziani P., Jovanović P., 2015, Ap&SS, 360, 7
Bon E., Marziani P., Berton M., Bon N., Antonucci R., Gaskell M., Ferland G., 2018, preprint (arXiv:1812.05828)
Boroson T. A., Green R. F., 1992, ApJS, 80, 109
Brotherton M. S., Wills B. J., Francis P. J., Steidel C. C., 1994, ApJ, 430, 495
Brown M. J. I., Duncan K. J., Landt H., Kirk M., Ricci C., Kamraj N., Salvato M., Ananna T., 2019, MNRAS, 489, 3351
Camps P., Baes M., 2020, Astron. Comput., 31, 100381
Chen B., Kantowski R., Dai X., Baron E., Maddumage P., 2015, ApJS, 218, 4
Collin S., Kawaguchi T., Peterson B. M., Vestergaard M., 2006, A&A, 456, 75
Corbett E. A., Robinson A., Axon D. J., Young S., 2000, MNRAS, 319, 685
Corbin M. R., 1995, ApJ, 447, 496
Czerny B., Hryniewicz K., 2011, A&A, 525, L8
Dalla Bontà E. et al., 2020, ApJ, 903, 112
Decarli R., Dotti M., Treves A., 2011, MNRAS, 413, 39
Doan A., Eracleous M., Runnoe J. C., Liu J., Mathes G., Flohic H. M. L. G., 2020, MNRAS, 491, 1104
Du P., Wang J.-M., 2019, ApJ, 886, 42
Emmanoulopoulos D., Papadakis I. E., McHardy I. M., Nicastro F., Bianchi S., Arévalo P., 2011, MNRAS, 415, 1895
Emmering R. T., Blandford R. D., Shlosman I., 1992, ApJ, 385, 460
ESO, 2019, Very Large Telescope Paranal Science Operations FORS2 User Manual. European Southern Observatory, VLT-MAN-ESO-13100-1543. Available at: http://www.eso.org/sci/facilities/paranal/instruments/fors/doc/VLT-MAN-ESO-13100-1543_P07.pdf
Fairall A. P., 1977, MNRAS, 180, 391
Feigelson E. D., Babu G. J., 1992, ApJ, 397, 55
Ferrarese L., Merritt D., 2000, ApJ, 539, L9
Fraix-Burnet D., Marziani P., D'Onofrio M., Dultzin D., 2017, Front. Astron. Space Sci., 4, 1
Frank J., King A., Raine D. J., 2002, Accretion Power in Astrophysics, 3rd edn. Cambridge Univ. Press, Cambridge
Gebhardt K. et al., 2000, ApJ, 539, L13
Gezari S., Halpern J. P., Eracleous M., 2007, ApJS, 169, 167
Goosmann R. W., Gaskell C. M., 2007, A&A, 465, 129
Greene J. E., Ho L. C., 2005, ApJ, 630, 122
Griersmith D., Visvanathan N., 1979, A&A, 79, 329
Haardt F., Maraschi L., 1993, ApJ, 413, 507
Hawley S. A., Phillips M. M., 1978, ApJ, 225, 780
Heiles C., 2000, AJ, 119, 923
Ishihara H., Takahashi M., Tomimatsu A., 1988, Phys. Rev. D, 38, 472
Jarvis M. J., McLure R. J., 2006, MNRAS, 369, 182
Kaspi S., Smith P. S., Netzer H., Maoz D., Jannuzi B. T., Giveon U., 2000, ApJ, 533, 631
Kennicutt Robert C. J., 1992, ApJS, 79, 255
Kollatschny W., 2003, A&A, 407, 461
Kollatschny W., Fricke K. J., 1985, A&A, 146, L11
Kormendy J., Ho L. C., 2013, ARA&A, 51, 511
Kormendy J., Richstone D., 1995, ARA&A, 33, 581
Koshida S. et al., 2014, ApJ, 788, 159
Kriss G., 1994, ASP Conf. Ser. Vol. 61, Astronomical Data Analysis Software and Systems III. Astron. Soc. Pac., San Francisco, p. 437
Kuraszkiewicz J. K., Green P. J., Crenshaw D. M., Dunn J., Forster K., Vestergaard M., Aldcroft T. L., 2004, ApJS, 150, 165
Laor A., Draine B. T., 1993, ApJ, 402, 441
Leighly K. M., Moore J. R., 2004, ApJ, 611, 107
Lin D. et al., 2017, Nat. Astron., 1, 0033
Lira P., Goosmann R. W., Kishimoto M., Cartier R., 2020, MNRAS, 491, 1
Lohfink A. M., Reynolds C. S., Miller J. M., Brenneman L. W., Mushotzky R. F., Nowak M. A., Fabian A. C., 2012, ApJ, 758, 67
Lohfink A. M. et al., 2016, ApJ, 821, 11
Loveday J., 1996, MNRAS, 278, 1025
Lub J., de Ruiter H. R., 1992, A&A, 256, 33
McConnell N. J., Ma C.-P., Gebhardt K., Wright S. A., Murphy J. D., Lauer T. R., Graham J. R., Richstone D. O., 2011, Nature, 480, 215
Marin F., 2018, A&A, 615, A171
Marin F., Goosmann R. W., Gaskell C. M., Porquet D., Dovčiak M., 2012, A&A, 548, A121
Marin F., Goosmann R. W., Gaskell C. M., 2015, A&A, 577, A66
Marinello M., Rodríguez-Ardila A., Marziani P., Sigut A., Pradhan A., 2020, MNRAS, 494, 4187
Marziani P., Sulentic J. W., 2012, New Astron. Rev., 56, 49
Marziani P., Sulentic J. W., Dultzin-Hacyan D., Calvani M., Moles M., 1996, ApJS, 104, 37
Marziani P., Sulentic J. W., Zwitter T., Dultzin-Hacyan D., Calvani M., 2001, ApJ, 558, 553
Marziani P., Sulentic J. W., Zamanov R., Calvani M., Dultzin-Hacyan D., Bachev R., Zwitter T., 2003a, ApJS, 145, 199
Marziani P., Zamanov R. K., Sulentic J. W., Calvani M., 2003b, MNRAS, 345, 1133
Marziani P., Sulentic J. W., Negrete C. A., Dultzin D., Zamfir S., Bachev R., 2010, MNRAS, 409, 1033
Marziani P. et al., 2018, Front. Astron. Space Sci., 5, 6
Marziani P. et al., 2019, A&A, 627, A88
Mauch T., Murphy T., Buttery H. J., Curran J., Hunstead R. W., Piestrzynski B., Robertson J. G., Sadler E. M., 2003, MNRAS, 342, 1117
Mejía-Restrepo J. E., Lira P., Netzer H., Trakhtenbrot B., Capellupo D. M., 2018, Nat. Astron., 2, 63
Mezcua M., Domínguez Sánchez H., 2020, ApJ, 898, L30
Nelson C. H., 2000, ApJ, 544, L91
Nelson C. H., Whittle M., 1996, ApJ, 465, 96
Oliva E., Origlia L., Kotilainen J. K., Moorwood A. F. M., 1995, A&A, 301, 55
Osterbrock D. E., Cohen R., 1979, MNRAS, 187, 61

Panda S., Czerny B., Adhikari T. P., Hryniewicz K., Wildy C., Kuraszkiewicz J., Śniegowska M., 2018, ApJ, 866, 115
Panda S., Marziani P., Czerny B., 2019, ApJ, 882, 79
Panda S., Martínez-Aldama M. L., Marinello M., Czerny B., Marziani P., Dultzin D., 2020, ApJ, 902, 76
Patat F., Romaniello M., 2006, PASP, 118, 146
Peterson B. M., 1993, PASP, 105, 247
Peterson B. M., Ferland G. J., 1986, Nature, 324, 345
Peterson B. M. et al., 2004, ApJ, 613, 682
Popović L. Č., 2020, Open Astron., 29, 1
Popović L. Č., Vince I., Atanacković-Vukmanović O., Kubičela A., 1995, A&A, 293, 309
Popović L. Č., Mediavilla E., Bon E., Ilić D., 2004, A&A, 423, 909
Press W. H., Teukolsky S. A., Vetterling W. T., Flannery B. P., 2007, Numerical Recipes: The Art of Scientific Computing, 3 edn. Cambridge Univ. Press, Cambridge
Proga D., 2003, ApJ, 592, L9
Punsly B., 2010, ApJ, 713, 232
Punsly B., Marziani P., Berton M., Kharb P., 2020, ApJ, 903, 44
Recondo-Gonzalez M. C., Wamsteker W., Clavel J., Rodriguez-Pascual P. M., Vio R., Ting-Gui W., Santos-Lleo M., Makino F., 1997, A&AS, 121, 461
Richards G. T., Vanden Berk D. E., Reichard T. A., Hall P. B., Schneider D. P., SubbaRao M., Thakar A. R., York D. G., 2002, AJ, 124, 1
Robinson A., Young S., Axon D. J., Kharb P., Smith J. E., 2010, ApJ, 717, L122
Rodriguez-Pascual P. M. et al., 1997, ApJS, 110, 9
Rojas Lobos P. A., Goosmann R. W., Marin F., Savić D., 2018, A&A, 611, A39
Rokaki E., Lawrence A., Economou F., Mastichiadis A., 2003, MNRAS, 340, 1298
Różańska A., Czerny B., 2000, A&A, 360, 1170
Runnoe J. C., Brotherton M. S., Shang Z., 2012, MNRAS, 427, 1800
Santos-Lleó M. et al., 1997, ApJS, 112, 271
Savić D., Goosmann R., Popović L. Č., Marin F., Afanasiev V. L., 2018, A&A, 614, A120
Savić D., Marin F., Popović L. Č., 2019, A&A, 623, A56
Savić D., Popović L. Č., Shablovinskaya E., Afanasiev V. L., 2020, MNRAS, 497, 3047
Schmoll S. et al., 2009, ApJ, 703, 2171
Shapovalova A. I. et al., 2016, ApJS, 222, 25
Shappee B. J. et al., 2014, ApJ, 788, 48
Shen Y., 2013, Bull. Astron. Soc. India, 41, 61
Shen Y., Ho L. C., 2014, Nature, 513, 210
Shen Y. et al., 2011, ApJS, 194, 45
Smith J. E., Young S., Robinson A., Corbett E. A., Giannuzzo M. E., Axon D. J., Hough J. H., 2002, MNRAS, 335, 773
Smith J. E., Robinson A., Alexander D. M., Young S., Axon D. J., Corbett E. A., 2004, MNRAS, 350, 140
Smith J. E., Robinson A., Young S., Axon D. J., Corbett E. A., 2005, MNRAS, 359, 846
Snedden S. A., Gaskell C. M., 2007, ApJ, 669, 126
Songsheng Y.-Y., Wang J.-M., 2018, MNRAS, 473, L1
Sulentic J. W., Marziani P., Dultzin-Hacyan D., 2000a, ARA&A, 38, 521
Sulentic J. W., Zwitter T., Marziani P., Dultzin-Hacyan D., 2000b, ApJ, 536, L5
Sulentic J. W., Marziani P., Zamanov R., Bachev R., Calvani M., Dultzin-Hacyan D., 2002, ApJ, 566, L71
Sulentic J. W., Zamfir S., Marziani P., Bachev R., Calvani M., Dultzin-Hacyan D., 2003, ApJ, 597, L17
Sulentic J. W., Bachev R., Marziani P., Negrete C. A., Dultzin D., 2007, ApJ, 666, 757
Sulentic J. W., Marziani P., del Olmo A., Dultzin D., Perea J., Negrete C. A., 2014, A&A, 570, A96
Thorne K. S., 1974, ApJ, 191, 507
Trakhtenbrot B. et al., 2019, Nat. Astron., 3, 242
Véron-Cetty M. P., Véron P., 2010, A&A, 518, A10
Vestergaard M., 2002, ApJ, 571, 733
Vestergaard M., Peterson B. M., 2006, ApJ, 641, 689
Walton D. J., Nardini E., Fabian A. C., Gallo L. C., Reis R. C., 2013, MNRAS, 428, 2901
Wang J., Li Y., 2011, ApJ, 742, L12
Wang Y., Li X.-D., 2012, ApJ, 744, 186
Wang J.-M., Du P., Li Y.-R., Ho L. C., Hu C., Bai J.-M., 2014, ApJ, 792, L13
Wang J.-M., Du P., Brotherton M. S., Hu C., Songsheng Y.-Y., Li Y.-R., Shi Y., Zhang Z.-X., 2017, Nat. Astron., 1, 775
Whittet D. C. B., Gerakines P. A., Hough J. H., Shenoy S. S., 2001, ApJ, 547, 872
Whittle M., 1992, ApJS, 79, 49
Wills B. J., Browne I. W. A., 1986, ApJ, 302, 56
Wolf J. et al., 2020, MNRAS, 492, 3580
Wu S.-M., Wang T.-G., Dong X.-B., 2008, MNRAS, 389, 213
Yan R. et al., 2016, AJ, 152, 197
Zamfir S., Sulentic J. W., Marziani P., Dultzin D., 2010, MNRAS, 403, 1759
Zheng W., Binette L., Sulentic J. W., 1990, ApJ, 365, 115
Zu Y., Kochanek C. S., Peterson B. M., 2011, ApJ, 735, 80

APPENDIX A: THE ESTIMATED BLACK HOLE MASS

A1 The inclination effect

In optical spectroscopy, we can observe only the line-of-sight velocity distribution of the BLR. Therefore, it is obvious that inclination of the BLR will play a significant role in the line width (Collin et al. 2006). Spectropolarimetry is a powerful tool to eliminate the inclination effect, since the intrinsic Keplerian velocity distribution can be obtained from the polarized profiles. The effect of inclination can be quantified by assuming that the line broadening is due to an isotropic component plus a flattened component, whose velocity field projection along the line of sight is $\propto 1/\sin i$, where i is the inclination of the system to the line of sight. Thus, the observed velocity distribution is:

$$\delta v_{obs}^2 = \frac{1}{3}\delta v_{\rm iso}^2 + \delta v_{\rm K}^2 \sin^2 i \tag{A1}$$

where $\delta v_{\rm iso}$ is an isotropic component, $\delta v_{\rm K}$ is the Keplerian velocity, and their ratio should be $\kappa = \delta v_{\rm iso}/\delta v_{\rm k} \gtrapprox 0.1$ (Collin et al. 2006; Marziani et al. 2018). In our work, we use the lower limitation of the ratio, i.e. $\kappa = 0.1$, and the $\delta v_{\rm obs}$ is the FWHM of the observed line profile from single epoch observations, i.e. $\delta v_{\rm obs} = {\rm FWHM}_{\rm obs}$.

Then the virial factor which relates black hole mass $M_{\rm BH}$ can be written as:

$$M_{\rm BH} = f_{\rm FWHM}\frac{R_{\rm BLR}}{G}{\rm FWHM}_{\rm obs}^2 \tag{A2}$$

where G is the gravitational constant, $R_{\rm BLR}$ is the radius of the BLR. $M_{\rm BH}$ is also related to the Keplerian velocity ${\rm FWHM}_{\rm k}$ as:

$$M_{\rm BH} = \frac{R_{\rm BLR}}{G}{\rm FWHM}_{\rm k}^2 \tag{A3}$$

Therefore the virial factor can be written as:

$$f_{\rm FWHM} = \frac{{\rm FWHM}_{\rm k}^2}{{\rm FWHM}_{\rm obs}^2} = \left[\frac{1}{3}\kappa^2 + \sin^2 i\right]^{-1} \tag{A4}$$

In the Fairall 9 case, the possible concurrence of a more complex geometry such as disc warping makes the interpretation of the width of the polarization profile uncertain. In order to measure the velocity dispersion associated with the Keplerian motion, we applied the decomposition technique (as mentioned before) to the Hβ and Hα polarized flux (Fig. A1). To estimate f, here we consider two different velocity FWHM of the Hβ and Hα profile in natural light: one

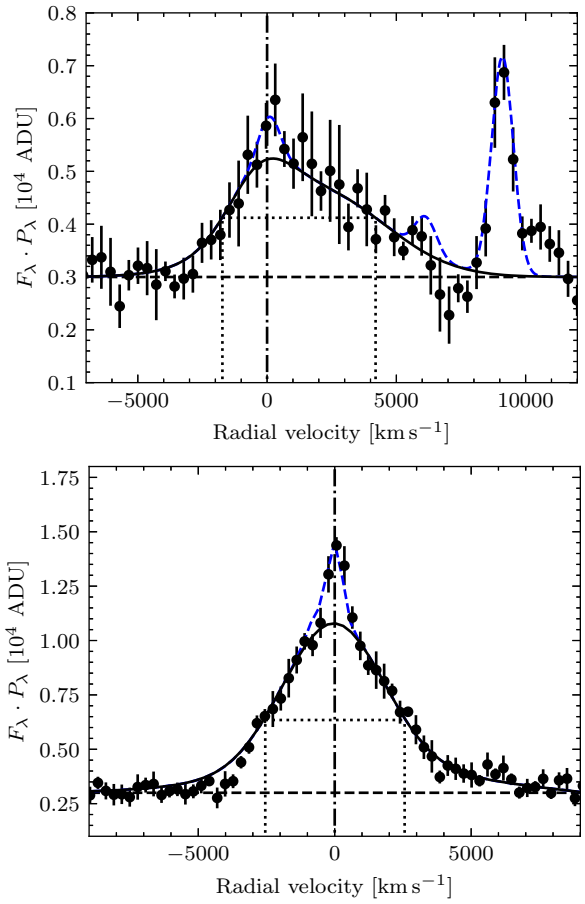

Figure A1. Top panel: black dots with error-bars at 1σ confidential level represent the polarized flux for H β. Black solid line shows the best fitting for the total broad polarized profile with two Gaussian components, with dotted lines showing the FWHM. Blue dashed lines represent the narrow polarized components. The continuum level is plotted in black dashed line. The zero radial velocity is marked with dot–dashed line. Bottom panel: same as top panel except for H α polarized profile.

Table A1. Inclination and virial factor estimation.

Line component	FWHM (F_λ) (km s^{-1})	FWHM ($P_\lambda \cdot F_\lambda$) (km s^{-1})	i (°)	f
(1)	(2)	(3)	(4)	(5)
H β BC	4010	5925	42.4	2.18
H β BC + VBC	5307	5925	63.3	1.25
H α BC	3848	5107	48.7	1.76
H α BC + VBC	5050	5107	80.8	1.02

Column 1: emission line and components in natural light used for the inclination and virial factor estimation. Column 2: FHWM of the components in natural light. Column 3: FWHM of the total broad profile in polarized light. Column 4 and 5: inclination and corresponding virial factor estimated with equation (A4), respectively.

associated with BC only and one with BC + VBC. The corresponding inclinations and virial factors are reported in Table A1. The BC FWHM is the parameter expected to be more strongly affected by orientation, and the f value derived for H β BC is the one used for the $M_{\rm BH}$ computation.

A1.1 Spectropolarimetric method

Several methods are being presently used to estimate the central black hole mass, starting from equation (A2). We consider first the spectropolarimetric data that can be used to estimate the black hole mass from the 'mark' of Keplerian motion on PA, in a way that is independent from the viewing angle (see Afanasiev & Popović 2015, for a detailed description of the method). In short, a rotating Keplerian BLR will produce a polarized light by equatorial scattering, where the PA of the polarization changes in a way that is correlated to the velocity field of the BLR. The relation between the velocity and the PA is (Afanasiev & Popović 2015; Afanasiev et al. 2019):

$$\log\left(\frac{V_i}{c}\right) = a - 0.5\log\left(\tan(\Delta {\rm PA}_i)\right) \quad \text{(A5)}$$

where c is the speed of light, and the ΔPA$_{\rm i}$ are the ones of Fig. A2. The slope is set to 0.5 to be consistent with the assumption of Keplerian motion within the BLR. The intercept a is a function of $M_{\rm BH}$ and can be written as

$$a = 0.5\log\left(\frac{GM_{\rm BH}\cos^2(\theta)}{c^2 R_{\rm sc}}\right) \quad \text{(A6)}$$

where G is the gravitational constant, $R_{\rm sc}$ is the inner radius of the scattering region, and θ is the angle between the BLR and the scatterer plane. Based on our assumption of equatorial scattering, θ should be very close to 0. However, it is worth noting that a non-coplanar torus has $\theta \sim$ 10–20°, and thus may introduce a systematic underestimate on $M_{\rm BH}$ at $\sim$ 10 per cent (Afanasiev & Popović 2015).

First, we verified that the slope is indeed consistent with a Keplerian velocity field. A bisector fit yields $b \approx -0.492 \pm 0.065$, consistent with the expected value $b = -0.5$. We then determined a by fitting the velocity and PA by linear regression (shown in Fig. A2). The estimated value is $a = -2.24 \pm 0.13$ for H β and -2.22 ± 0.15 for H α (with uncertainties at 1σ confidence level). To estimate the inner radius of the scattering region, we apply two techniques. First, we consider the dust lag-luminosity correlation described in Koshida et al. (2014) that yields the following relation between the time lag in K band (days) and the luminosity in V band:

$$\log \Delta t_{\rm K} = a_{\rm s} + b_{\rm s} M_{\rm V} \quad \text{(A7)}$$

where $a_{\rm s} = -2.11 \pm 0.04$. and $b_{\rm s} = -0.2$, both given by Koshida et al. (2014). Fairall 9 is known as variable source (Santos-Lleó et al. 1997), with secular trends superimposed to shorter time-scale variation of a significant amplitude. We consider here the $V \approx$13.36 for the nucleus of Fairall 9 provided by Griersmith & Visvanathan (1979), at an epoch when the AGN was reputed to be in a 'bright' phase. The corresponding V absolute magnitude is $M_{\rm V} = -23.0$, after applying a correction because of Galactic extinction ($A_{\rm V} \approx$ 0.071). Here, we assume that the time lag reflects the inner radius of the scattering region, i.e. $R_{\rm sc} = c\Delta t_K \approx$ 310 light d. Using equation (A6), we can estimate the black hole mass, which is shown in Table A2(a).

The radius of the scattering region $R_{\rm sc}$ can also be estimated following Afanasiev et al. (2019) who define a relation between FUV observations and $R_{\rm sc}$ from GALEX observations. The specific at 1516 Å for a 7 arcsec aperture is ≈3.08 mJy. Trouble is, the far-UV flux of Fairall 9 is strongly variable. The *IUE* average flux obtained during the reverberation mapping campaign of Fairall 9 by Rodriguez-Pascual et al. (1997) are consistent with the *GALEX* values, but the rms is ≈ 30 per cent, with the source doubling in flux on a time-scale of 6 month. Applying the relation of Afanasiev et al.

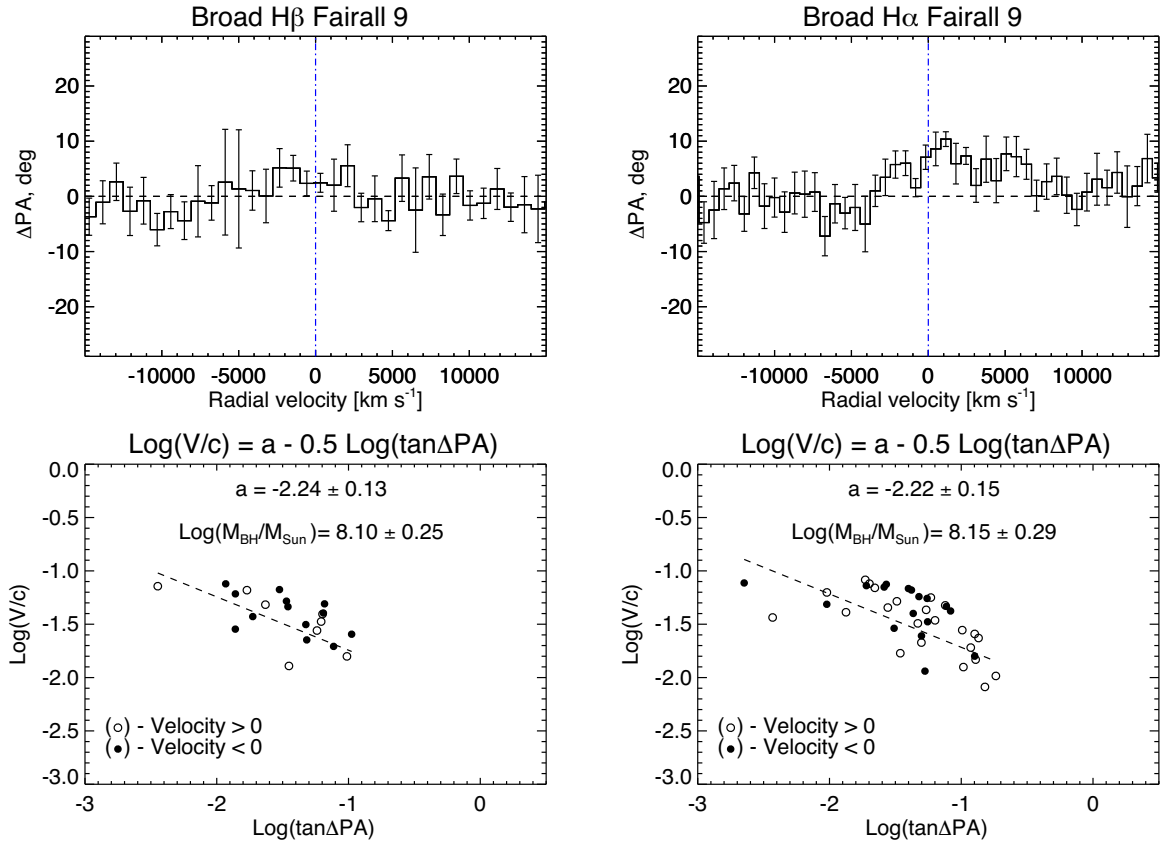

Figure A2. The polarization angle profiles for H β (left) and H α (right) lines. On the upper panels, the deviation of the polarization angle to the mean value (horizontal dashed line) is given. The maximum ΔPA is 6° for H β and 10° for H α. The vertical dashed lines mark the center of the emission lines. The grey shaded area show the contamination of the [O III] emission for H β and the atmospheric B band absorption for H α, respectively. The bottom panels show the relation of log (v_r/c) vs log (tan ΔPA). The $M_{\rm BH}$ shown here is estimated assuming $R_{\rm sc} = 215$ light d.

(2019) after extinction correction, we obtain $R_{\rm sc} \approx 215$ light d. This second $M_{\rm BH}$ estimate is also reported on Table A2(a).

A1.2 Other methods

A1.2.1 The RM method The RM method is based on the response of the broad emission lines to the continuum variations. Reliable estimates of the lag between the continuum and the H β broad emission line light curves for over 100 AGNs are presently available (Du & Wang 2019, and references therein). The rest-frame time lag in H β obtained using cross-correlation function (CCF) by Peterson et al. (2004) is $\tau = 17.4^{+3.2}_{-4.3}$ d. Alternatively, the rest-frame lag can be derived with a statistical technique called Just Another Vehicle for Estimating Lags In Nuclei [JAVELIN; Zu, Kochanek & Peterson 2011, formerly known as Stochastic Process Estimation for AGN Reverberations (SPEAR)]. RM provides the line emitting region radius that can be entered in equation (A2). The measured line width for the full H β profile is FWHM(H β) $= 4010 \pm 18$ km s^{-1}. The H β lines has been studied in the past as the major virial broadening estimator for $M_{\rm BH}$ computation. In order to compute $M_{\rm BH}$, we use velocity dispersion measures for the BC with corresponding virial factors, and with time lag obtained using different techniques. The final results for $M_{\rm BH}$ are reported in Table A2(b).

The AGN Black Hole Mass Database (Bentz & Katz 2015) reports the values of radii and line width measurements on the rms spectra from the optical and UV reverberation mapping campaigns (Santos-Lleó et al. 1997; Rodriguez-Pascual et al. 1997). The last entry in Table A2(b) refer to the H β rms dispersion σ, with a $f \approx 3.76$.

A1.2.2 The R–L scaling relations The RM observations of more than 70 AGNs so far have led to an empirical correlation between radius of the BLR and the luminosity of the continuum, i.e. the RL relation (Kaspi et al. 2000; Bentz et al. 2009). This relation has made possible single-epoch $M_{\rm BH}$ estimations for large samples of quasars: $M_{\rm BH}$ is derived just from the continuum (or emission line) luminosity and line width of single-epoch spectroscopy (Vestergaard 2002; Vestergaard & Peterson 2006; Greene & Ho 2005). In Table A2(c), the luminosity of the continuum at 5100 Å is obtained from Bentz et al. (2009), which already has the host contamination subtracted. The nucleus luminosity of H β BC is derived from Marziani et al. (2003a), and the luminosity of H α is converted from L_{5100} using the empirical relation given by Greene & Ho (2005).

A1.2.3 The $M_{BH} - \sigma_\star$ *relation* The $M_{\rm BH}$ and the stellar velocity dispersion ($\sigma_\star$) in the host galaxy bulge has been found to be strongly correlated (Ferrarese & Merritt 2000; Gebhardt et al. 2000; Nelson 2000). However, for luminous Seyfert 1 galaxies like Fairall 9 it is relatively difficult to detect the virial motion in the host galaxy. Nelson & Whittle (1996) have found a strong correlation between $\sigma_\star$ and the FWHM of [O III]λ5007 for the majority of Seyfert galaxies, indicating that the [O III]λ5007 profile is dominated by virial motion in the bulge potential. Therefore we use $\sigma_\star = {\rm FWHM}_{\rm [O\,III]}/2.35$

Table A2. $M_{\rm BH}$ Estimates.

(a) Spectropolarimetry

Line	M_V (mag)	$L_{\rm GALEX}(1516)$ (10^{44} erg s^{-1})	$R_{\rm sc}$ (light d)	a	$\cos\theta$	$M_{\rm BH}$ ($10^7 M_\odot$)	Notes/Refs.
(1)	(2)	(3)	(4)	(5)	(6)	(7)	(8)
H β	–	2.75	215	-2.24 ± 0.13	$\sim$1	12.5 $\pm$ 7.5	Afanasiev et al. (2019), Feigelson & Babu (1992)
H β	-23.0	–	310	-2.24 ± 0.13	$\sim$1	18.2 $\pm$ 10.8	Afanasiev & Popović (2015), Koshida et al. (2014)
H α	–	2.75	215	-2.22 ± 0.15	$\sim$1	13.7 $\pm$ 9.5	Afanasiev et al. (2019), Feigelson & Babu (1992)
H α	-23.0	–	310	-2.22 ± 0.15	$\sim$1	19.8 $\pm$ 13.6	Afanasiev & Popović (2015), Koshida et al. (2014)

(b) Virial - $r_{\rm BLR}$ from H β RM

Line component	f	$R_{\rm BLR}$ (light d)	FWHM (km s^{-1})	$M_{\rm BH}$ ($10^7 M_\odot$)	Lag technique	Lag Ref
(1)	(2)	(3)	(4)	(5)	(6)	(7)
H β BC	2.18	$17.4^{+3.2}_{-4.3}$	4010 $\pm$ 18	$11.9^{+2.2}_{-2.9}$	CCF	Peterson et al. (2004)
H β BC	2.18	$19.4^{+42.1}_{-3.8}$	4010 $\pm$ 18	$13.3^{+28.8}_{-2.6}$	JAVELIN	Zu et al. (2011)
H β rms $\sigma^\dagger$	3.76	$17.4^{+3.2}_{-4.3}$	3787 $\pm$ 197	$18.3^{+3.9}_{-4.9}$	CCF	Peterson et al. (2004)

(c) Scaling laws

Relation	FWHM (km s^{-1})	L (10^{44} erg s^{-1})	$M_{\rm BH}$ ($10^7 M_\odot$)	Relation Ref
(1)	(2)	(3)	(4)	(5)
FWHM$_{\rm H\beta}$, L_{5100}	4010 $\pm$ 18	1.38 $\pm$ 0.08	15.4 $\pm$ 0.8	Vestergaard & Peterson (2006)
FWHM$_{\rm H\alpha}$, L_{5100}	3847.8 $\pm$ 9.6	1.38 $\pm$ 0.08	24.1 $\pm$ 1.4	Bentz et al. (2009), Assef et al. (2011)
FWHM$_{\rm H\alpha}$, $L_{\rm H\alpha}$	3847.8 $\pm$ 9.6	0.15 $\pm$ 0.01	31.7 $\pm$ 6.5	Greene & Ho (2005), Shen et al. (2011)

(d) $M_{\rm BH}-\sigma_\star$ correlation

Samples	$\sigma_\star$ (km s^{-1})	Line	$M_{\rm BH}$ ($10^7 M_\odot$)	$\sigma_\star$ Ref
(1)	(2)	(3)	(4)	(5)
Entire	215 $\pm$ 20	Si(1.59 μm)	28.2 $\pm$ 15.5	Oliva et al. (1995)
Entire	181 $\pm$ 10	[O III]λ5007	11.7 $\pm$ 3.7	Whittle (1992)
Early-type	215 $\pm$ 20	Si(1.59μm)	33.3 $\pm$ 16.1	Oliva et al. (1995)
Early-type	181 $\pm$ 10	[O III]λ5007	15.2 $\pm$ 4.4	Whittle (1992)

Notes. (a) $M_{\rm BH}$ estimated with spectropolarimetric data using equation (A6). Column 1: emission line for mass estimation. Column 2: absolute magnitude in V band transformed from the nuclear apparent magnitude measured by Griersmith & Visvanathan (1979). Column 3: *GALEX* luminosity at 1516 Å. Column 4: radius of the scattering region estimated with equation (A7; second and fourth rows) or Afanasiev et al. (2019) method (first and third rows). Column 5: intercept of the linear regression as shown Fig. A2. Column 6: cosine of the angle θ between BLR plane and the inner scattering region, which is assumed to be close to 1($\theta \sim 0$). Column 7: the estimated black hole mass with uncertainties at 1σ confidential level. Column 8: references for the apparent magnitude, *GALEX* luminosity, and their relation with $R_{\rm sc}$.
(b) Column 1: emission line and component. Column 2: virial factor for corresponding line component (see Table A1). Column 3: radius of the BLR obtained using different techniques. Column 4: FWHM for different lines. The value for H α has been rescaled to the correlating H β width. Column 5: black hole mass estimated with equation (A2). Column 6: techniques for obtaining the time lags. Column 7: references for the lags.
(c) Single epoch $M_{\rm BH}$ estimated with scaling relations. Column 1: empirical relations between the emission line FWHM and the luminosity. Column 2: emission line FWHM. Column 3: luminosity of the continuum or emission line. Column 4: the estimated $M_{\rm BH}$. Column 5: references for the luminosity and the scaling relation.
(d) $M_{\rm BH}$ estimated with the empirical $M_{\rm BH}-\sigma_\star$ correlation. The empirical $M_{\rm BH}-\sigma_\star$ correlation of McConnell et al. (2011) is provided for three different samples analysed in their work. Column 1: samples for regression in McConnell et al. (2011). Column 2: stellar dispersion. Column 3: emission/absorption line for stellar dispersion estimation. Column 4: the estimated $M_{\rm BH}$. Column 5: references of the emission/absorption line dispersion.
†As reported in the AGN Black Hole Mass Database (Bentz & Katz 2015).

where FWHM$_{\rm [O\,III]} = 425$ km s^{-1} is measured by Whittle (1992) with the instrumental effects corrected. The only direct stellar velocity dispersion measurement we are aware of: Oliva et al. (1995) found 228 ± 20 km s^{-1} from the mid-IR feature of Si at 1.59 μm. The values are consistent but the IR value needs to be carefully calibrated, as a small difference can yield to a large mass difference. In order to determine the correlation between $M_{\rm BH}$ and $\sigma_\star$, previous work carried out by McConnell et al. (2011) separated the entire sample of 65 local galaxies into two sub-samples (early-type and late-type) based on their morphology. We report in Table A2(d) the $M_{\rm BH}$ estimates based on the early-type, late-type and entire sample scaling laws of McConnell et al. (2011), although the scaling law derived for the entire sample should be preferred because of a better statistics.

APPENDIX B: POLARIZATION MODELING

In order to investigate various effects of different BLR geometry and kinematics on the polarization spectra, we performed three

simulations using radiative transfer codes STOKES[6] (Goosmann & Gaskell 2007; Marin et al. 2012; Marin, Goosmann & Gaskell 2015; Marin 2018; Rojas Lobos et al. 2018) and SKIRT[7] (Baes et al. 2019; Camps & Baes 2020, and references therein). We assumed that the BLR emission is being scattered by the inner part of the dusty torus. We assumed three different geometries of the BLR: disc-like, bi-conic, and spherical (Fig. B1).

The velocity field for each BLR geometry was chosen respectively as Keplerian, radial outflows and random motion. The inner radius of the BLR was taken from the RM measurements as the mean value: $R_{\rm in}^{\rm BLR} = 18$ ld. The BLR outer radius was calculated based on bolometric luminosity $R_{\rm out}^{\rm BLR} = 0.2 L_{46}^{0.5}$ pc $= 70$ ld (Laor & Draine 1993). The bolometric luminosity was calculated from optical luminosity L_{5100} (Runnoe, Brotherton & Shang 2012). The inner radius of the scattering region $R_{\rm in}^{\rm SR} = 262$ ld was estimated from the UV $L_{\rm GALEX}(1516)$ (Afanasiev et al. 2019). The outer radius of the SR was taken as the distance in the equatorial plane from which the half-opening angle of the outer edge of the BLR is viewed at the angle of 25°, i.e. $R_{\rm out}^{\rm SR} = R_{\rm out}^{\rm BLR} / \sin 12.5^\circ = 322$ ld (same as it was done by Savić et al. 2018). The total radial depth of the SR is set to unity. The SMBH mass was set to $M_{\rm BH} = 2 \times 10^8\,{\rm M}_\odot$. All parameters of the model using the mean value of each observable given in Table A2. For every simulation, we used one BLR configuration while keeping the same SR. Each of the BLR configuration has the same inner and outer radius.

In Fig. B2 (due to azimuthal symmetry), we show the profiles of the total unpolarized flux (top panels), polarized flux $p \times F$ (top second panels), Stokes parameters Q (top third panel), U (top fourth panels), the degree of linear polarization p (top fifth panels), and PA(bottom panels) for the disc-like, bi-conic, and spherical BLR geometry (from left to right, respectively).

A warped disc was modeled as two discs: the inner and the outer. The inner disc was set from 1000 to 2000 $r_{\rm g}$ and rotated along the x-axis for 30°. The outer disc continues from 2000 $r_{\rm g}$ up to 10 000 $r_{\rm g}$ Fig. B1 (bottom panels). The system is viewed at an inclination $i =$ 15° and at azimuthal angles $\phi = 0^\circ,\ 22.5^\circ\ 45^\circ$ and 90°. Polarization profiles for the two disc model is shown in Fig. B3.

[6] http://www.stokes-program.info
[7] https://skirt.ugent.be/root/_landing.html

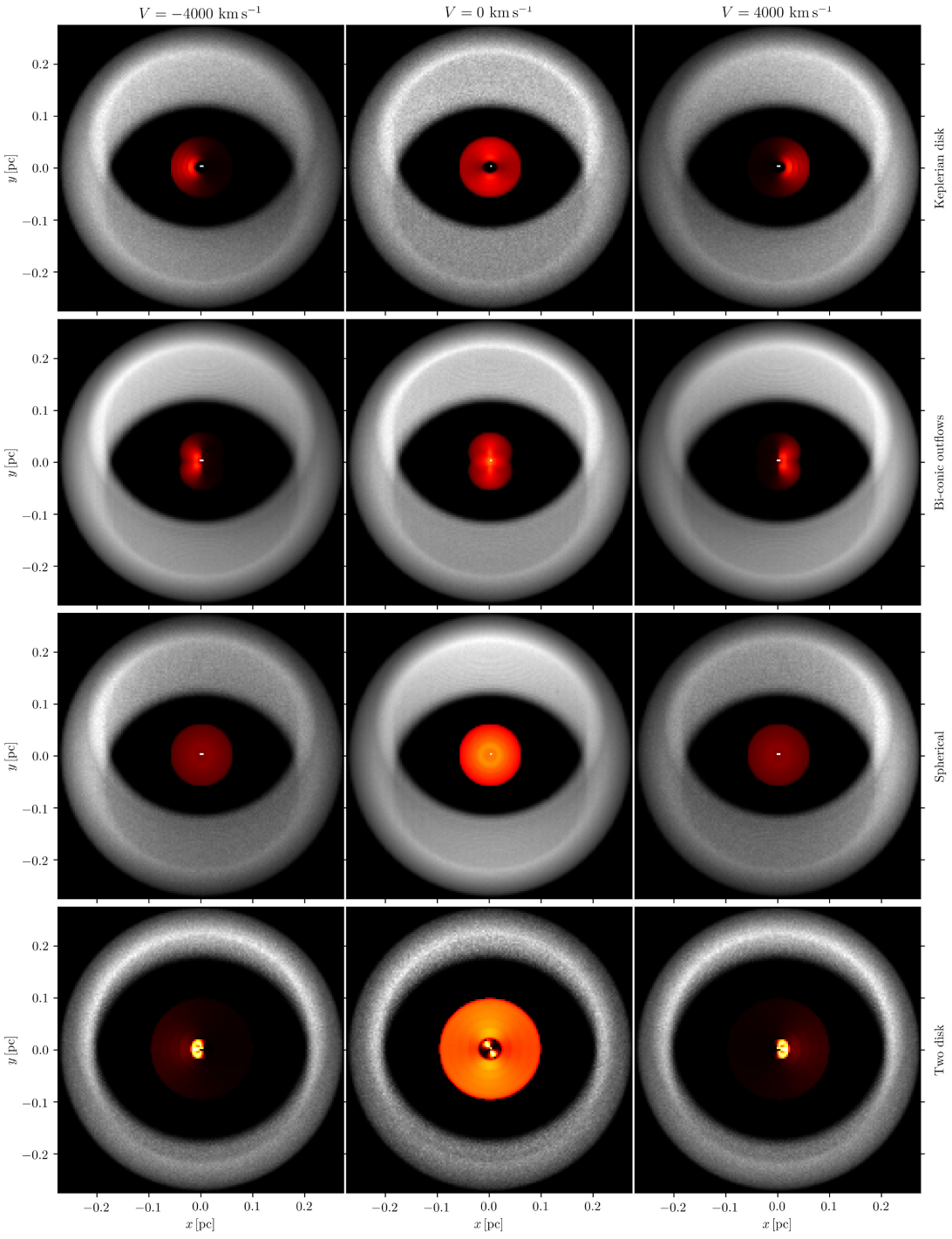

Figure B1. Geometric setup of our models. BLR geometry from top to bottom: Keplerian disc, double-cone, spherical, and two disc model. From left to right: radiation emitted at V $= -4000$, 0, and 4000 km s^{-1}. The scattering region is shown in grey. The point source approximates the accretion disc emission. All the models except the two disc model are viewed at an inclination of 25°. The two disc model is viewed at an inclination of the outer disc 15° and azimuth $\phi = 45°$.

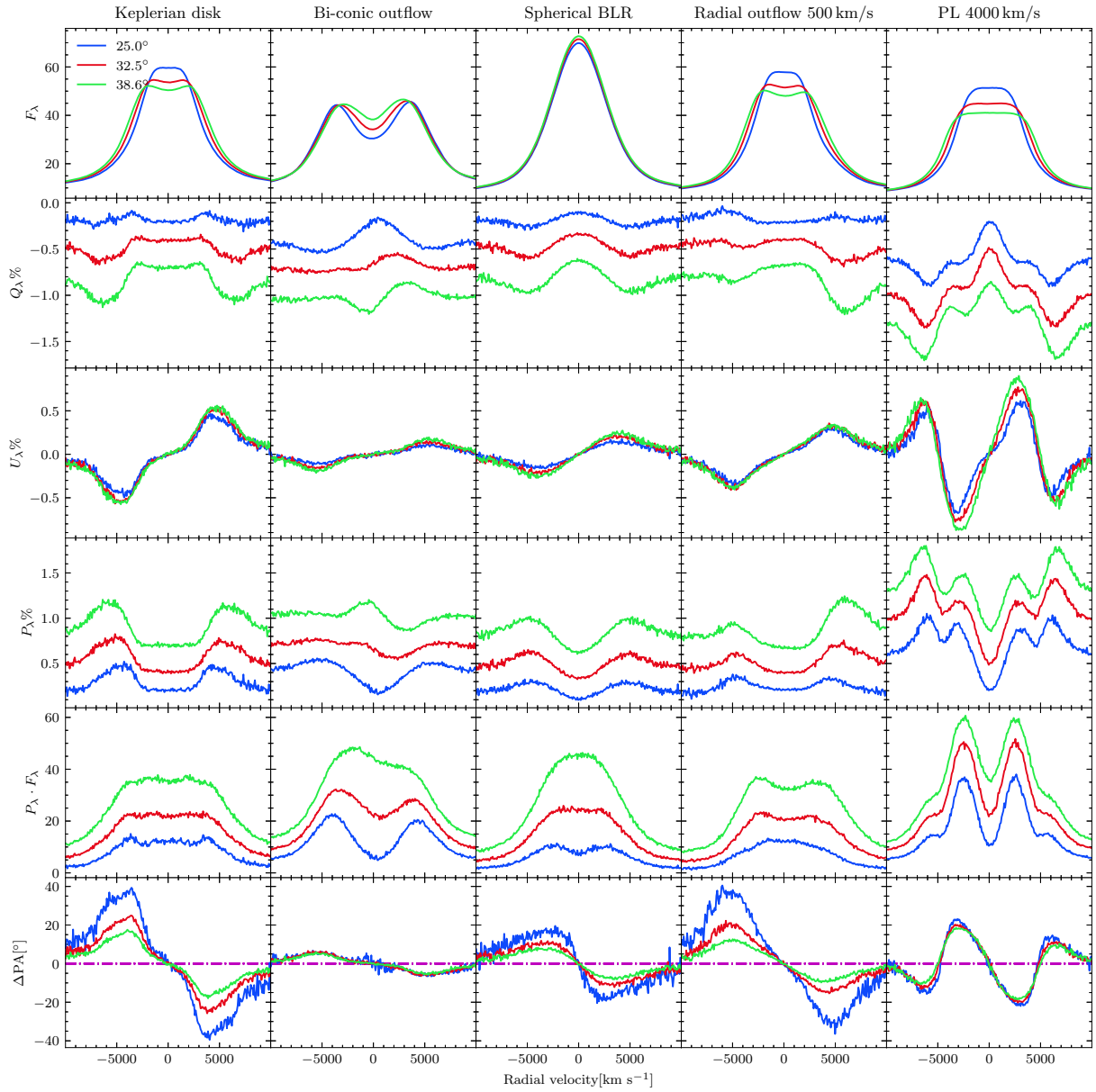

Figure B2. Polarization parameters for three of the models (Keplerian disc, bi-conical outflow, and spherical BLR) considered in this work, at three different inclination values: total unpolarized flux (top row), polarized flux (second from top), Stokes parameters Q_λ and U_λ, degree of linear polarization P_λ (second row from bottom), and polarization PA (bottom).

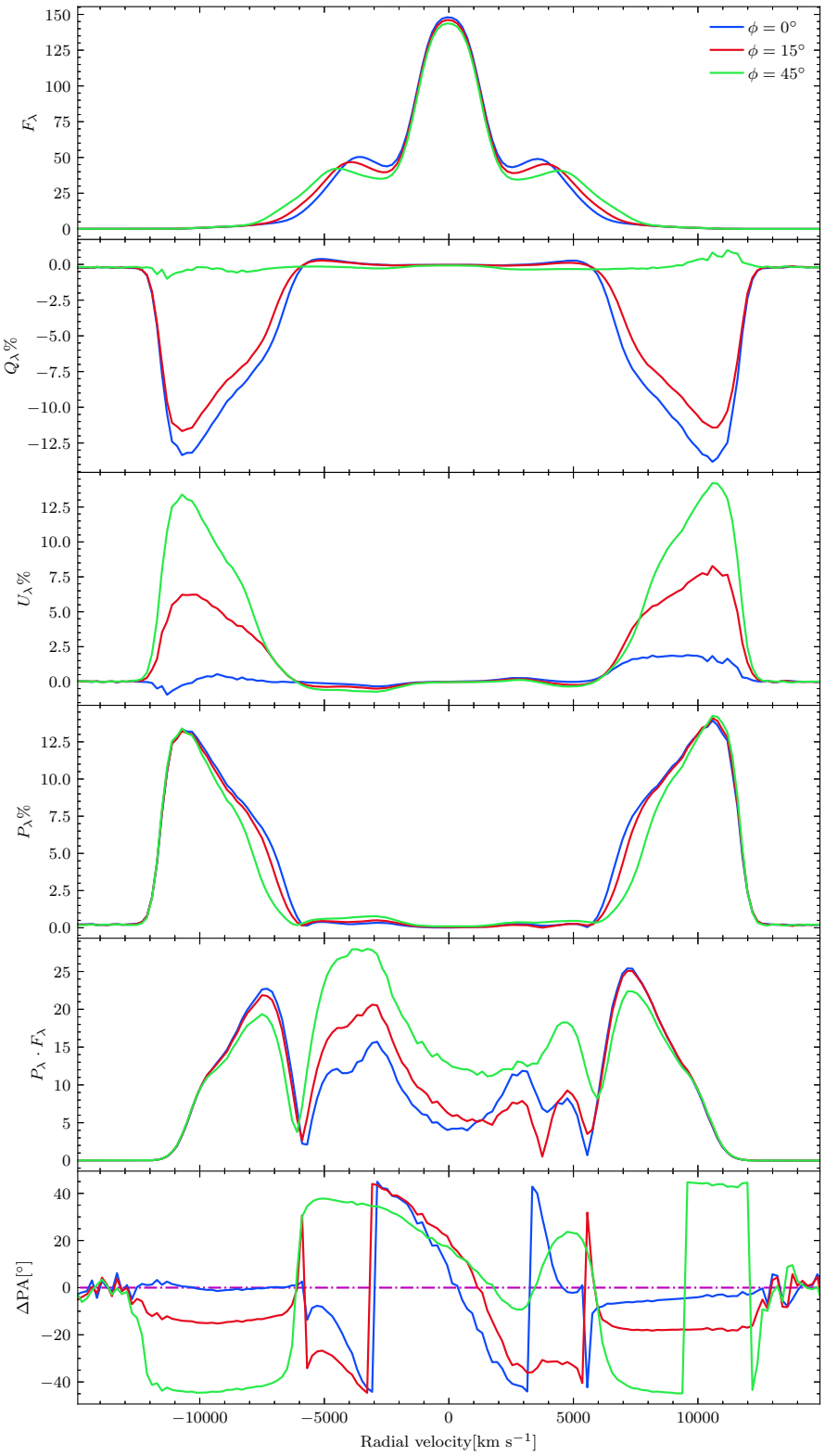

Figure B3. Same as Fig. B2, but for the two disc model. The system is viewed at inclination $i = 15°$ and azimuth $\phi = 0°,\ 15°$, and $45°$ (blue, red, and green lines, respectively).

This paper has been typeset from a TEX/LATEX file prepared by the author.